Improving Beamforming-based Methodologies for Seismological Analysis

by

Fengzhou Tan
B.Sc., Peking University, 2017

A Thesis Submitted in Partial Fulfillment of the
Requirements for the Degree of

MASTER OF SCIENCE

in the School of Earth and Ocean Sciences

Supervisory Committee

Improving Beamforming-based Methodologies for Seismological Analysis

by

Fengzhou Tan
B.Sc., Peking University, 2017

Supervisory Committee

Dr. Edwin Nissen, Co-Supervisor
School of Earth and Ocean Sciences

Dr. Honn Kao, Co-Supervisor
School of Earth and Ocean Sciences

Dr. Stan Dosso, Departmental Member
School of Earth and Ocean Sciences

Abstract

We improved two beamforming-based methodologies for seismological analysis. The first one is a new Three-Dimensional Phase-Weighted Relative Back Projection (3-D PWBP) method to improve the spatial resolution of Back Projection results. We exploit both phase and amplitude of the seismogram signal to enhance the distinction of correlated signals. Also, we implement a 3-D velocity model to provide more accurate travel times. We vindicate these refinements with several synthetic tests and an analysis of the 1997 M_w 7.2 Zirkuh (Iran) earthquake, which we show ruptured mainly unilaterally southwards at a rupture speed of ∼3.0 km/s along its ∼125 km-long, mostly single-stranded surface rupture. Then, we apply the new method to the more complex case of the 2016 M_w 7.8 Kaikōura (New Zealand) earthquake, which we demonstrate is divided into two major stages separated by a gap of ∼8 s and ∼30–40 km. The overall rupture speed is ∼1.7 km/s and the overall duration is ∼84 s, considerably shorter than some earlier estimates. We see no clear evidence for continuous failure of the subduction interface that underlies the known, surface-rupturing crustal faults, though we cannot rule out its involvement in the second major stage in the northern part of the rupture area. The late (∼80 s) peak in relative energy is likely a high-frequency stopping phase, and the rupture appears to terminate southwest of the offshore Needles fault.

The second methodology is a novel workflow for earthquake detection and location, named Seismicity-Scanning based on Navigated Automatic Phase-picking (S-SNAP). By taking a cocktail approach that combines Source-Scanning, Kurtosis-based Phase-picking and the Maximum Intersection location technique into a single integrated workflow, this new method is capable of delineating complex spatiotemporal distributions of seismicity. It is automatic, efficiently providing earthquake locations with high comprehensiveness and accuracy. We apply S-SNAP to a dataset recorded by a dense local seismic array during a hydraulic fracturing operation to test this novel approach and to demonstrate the effectiveness of S-SNAP in comparison to existing methods. Overall, S-SNAP found nearly four times as many high-quality events as a template-matching based catalogue. All events in the previous catalogue are identified with similar epicenter, depth and magnitude, while no false detections are found by visual inspection.

Table of Contents

List of Tables

List of Figures

Acknowledgements

I would like to thank my supervisors, Edwin Nissen and Honn Kao, for their help during my master study. Also, I thank Zengxi Ge and David Eaton for their contributions to the research projects included in this thesis. And I thank the editors of the Geophysical Journal International and two anonymous reviewers for their helpful comments on the back projection study.

I thank my committee member Stan Dosso and external examiner Andrew Schaeffer for their encouragement and suggestions to the thesis.

This study also benefited from constructive discussions with Eric Bergman, Ezgi Karasözen, Nadine Igonin and Zhipeng Liu.

I thank Chenxu Chen and Guanzhi Wang for helping develop the BP program used in this study, and Connor Gaudreau for helping develop the parallel-computing portion of the S-SNAP program used in this study.

Part of the seismic data were obtained from the IRIS data center. Continuous raw data used in S-SNAP (geophone and broadband recordings, network code TC2ME) are available, following a holdback period that expires on 1 July 2020, through the IRIS data center at http://ds.iris.edu/mda/5B?timewindow=2016-2017. The ToC2ME program was enabled by generous support from two companies.

Some of the figures were created using the Generic Mapping Tools (GMT) software (Wessel et al., 2013).

This research was partially supported by the National Natural Science Foundation of China (NSFC) grant 41774047 (ZG), Natural Sciences and Engineering Research Council of Canada (NSERC) Discovery grants RGPIN 418268-2013 (HK) and 2017 04029 (EN), the Energy Innovation Program of Natural Resources Canada (HK), a University of Victoria Graduate Fellowship (FT) and a Canada Research Chair (EN).

In addition, I'd like to thank other scientists in University of Victoria and Pacific Geosciences Centre and other institutes for their help during my master study. And I thank my family and friends for their love, kindness, encouragement and help.

Chapter 1 Thesis Overview

About half a century ago, the beamforming system was designed to output a single coherent wave generated by multiple sources (Barry, 1968; Rusnak, 1969). The principle of this technique is to compensate different phase delays in different sources. Conversely, the beamforming technique can be used to identify a signal from a particular direction from noise and other interfering signals with an array (Veen & Buckley, 1988). In seismological analysis, given a known epicenter and a seismic array, applying different slowness to calculate phase delays in beamforming results in enhancement of different seismic phases (Rost & Thomas, 2002).

Recently, the beamforming technique has been modified into many more seismological methods, sharing the idea of shifting and stacking. In large earthquakes, the rupture process can be characterized as a sequence of subevents at varying locations, which cause different phase delays at particular stations in a teleseismic array. Back Projection (BP) exploits this by aligning seismograms according to a grid of locations to distinguish these subevents in space and time (Ishii et al., 2005). It also relies on cross correlation to force the alignment at the hypocenter, compensating for unknown path anomalies that are shared by the whole array. Consequently, this method has limitations when the first subevent or hypocenter is unknown or when waveforms lack similarity due to different structures along the ray paths.

Other cases where traditional earthquake location methods fail include non-volcanic tremor and aftershock sequences. The former doesn't have clear onsets necessary for traditional location, while the latter may exhibit chaotic clusters of onsets in short time intervals. The Source Scanning Algorithm (SSA) builds upon array beamforming by utilizing stations at all azimuths (Kao & Shan, 2004). It only stacks the absolute values of amplitude, which allows seismograms without similarity but belonging to the same source to be considered. This modification makes it possible to use local arrays to study small but chaotic sequences of energy releases, such as tremor (Kao & Shan, 2004) and aftershocks (Liao et al., 2012).

The aforementioned methods, BP and SSA, are both based on beamforming and seeking better understanding of how seismic energy is released in time and space. At larger spatial scales, BP gives important information about rupture propagation direction, speed, length and duration. Higher resolution rupture histories would make it possible to see in more detail where and when the rupture nucleates, accelerates (or decelerates), jumps, and terminates. This could provide important information for learning earthquake mechanisms, such as why the rupture stops or continues in certain places, whether the rupture accelerates or decelerates in weak zones, and in which conditions the rupture can jump through a barrier, triggering other faults to slip or leaving a gap along the fault.

At finer spatial scales, SSA provides the spatiotemporal distribution of earthquakes and tremors in a local or regional scale. Where and when tremors happen is crucial for studying subduction zones and for understanding the mechanics and rheology of megathrust faults capable of generating large earthquakes and tsunamis. Aftershock sequences provide vital constraints on fault mechanics and interactions during and after the major energy release. With comprehensive catalogs, especially quickly and accurately generated by machines, it will be possible to compare the aftershock sequences across the world and look for energy release patterns. Also, we could dig into the physics of induced seismicity, for example, where and how long are the active or reactivated faults nearby, and where and when would a big earthquake happen based on the observation of thousands of small ones.

All aforementioned questions are closely related to seismic hazard mitigation yet still poorly understood, limiting progress in earthquake rupture forecasting and early warning. Thus, we need better and more observations with higher resolution and accuracy to gain a better picture of earthquake sources. In this thesis, we propose two new methodologies based on the beamforming technique to observe seismic energy release.

In chapter 2, we introduce the 3-D Phase-Weighted Relative Back Projection method (3-D PWBP) that improves the spatiotemporal resolution of BP results by exploiting both phase and amplitude of the seismic signal with a 3-D velocity model. We validate the advantage of these refinements with synthetic tests and an analysis of the 1997 Mw 7.2 Zirkuh (Iran) earthquake. As an application of this method, we analyze the more complex 2016 M_w 7.8 Kaikōura (New Zealand) earthquake, widely recognized as one of the most complex earthquakes ever recorded.

In chapter 3, we detail a novel approach for automatic earthquake detection and location, named Seismicity-Scanning based on Navigated Automatic Phase-picking (S-SNAP). We provide tests with a dataset recorded by a dense local seismic array during a hydraulic fracturing operation to demonstrate the effectiveness of S-SNAP in comparison to existing methods.

Finally, in chapter 4, we discuss the potential applications of these two new methods and future works.

Chapter 2 Validation of the 3-D PWBP Technique and its Application to the 2016 M_w 7.8 Kaikōura Earthquake

2.1 Introduction

Large earthquake ruptures can reach hundreds of kilometers in extent and last tens to hundreds of seconds. Mapping seismic energy release in time and space is key to understanding the processes by which these ruptures evolve and eventually terminate. Finite fault models map the progression of slip across a fault plane or fault planes through time (Wald & Heaton, 1994), but depend upon an assumption of which nodal plane represents the fault, or, for more complex events, upon independent constraints on fault geometry such as from geodetic data. This information can take time to emerge and may not fully distinguish coseismic from post-seismic deformation. In contrast, back projection (BP) methods image the rupture process using only the epicenter and depth as prior constraints (Ishii et al., 2005). This offers a distinct advantage for imaging complex, multi-fault ruptures, particularly in the immediate aftermath of an event.

A suite of BP variants has emerged over the past decade, which can be roughly divided into those undertaken in the time domain, such as Relative Back Projection (RBP) (Zhang & Ge, 2010), n-th Root Back Projection (Xu et al., 2009) and Cross-Correlation Back Projection (CCBP) (Ishii, 2011), and those in the frequency domain, such as Multiple Signal Classification (MUSIC) BP (Meng et al., 2011; Meng, Ampuero, Luo, et al., 2012) and Compressive Sensing (CS) (Yao et al., 2011). The accuracy of these methods mainly depends on the veracity of the theoretical travel times, the extraction of the relevant signal from the noise, and the exclusion of other seismic disturbances. To improve the accuracy of travel times, well-located aftershocks can be used for correction (Ishii et al., 2007) and a three-dimensional (3-D) earth velocity model can be used instead of a one-dimensional (1-D) model (Liu et al., 2017, 2018). Weak signals may be identified and enhanced using n-th root stacking (Xu et al., 2009), phase-weighted stacking (Wang et al., 2017), semblance-weighted stacking (Vallée et al., 2008) or cross-correlation (CC) coefficients (Ishii, 2011) instead of linear stacking. Interference from other phases can be reduced using the Imaging Deconvolution Back Projection method, by tracing back a suite of phases (such as near-source depth phases pP and sP) to a single subevent (D. Wang et al., 2016). In addition, artefacts can be mitigated by using global data that incorporate arrays at different azimuths (Liu & Ge, 2015; Zhang et al., 2017).

Schimmel and Paulssen (1997) and Rost and Thomas (2002) showed that phase-weighted stacking is better than linear stacking or CC coefficients for signal extraction, and performs at least equally well as the n-th root stacking. Whereas n-th root stacking uses only amplitude to emphasize the signal coherence, phase carries important additional information about the source process, making phase-weighted stacking a logical extension. Although phase-weighted stacking was used in mapping the 2015 M_w 7.9 Gorkha (Nepal) earthquake rupture process (Wang et al., 2017), exactly how it was implemented under the framework of BP was not explained in detail. Furthermore, there was no comprehensive assessment on how much improvement phase-weighted stacking can achieve with respect to other stacking schemes. Therefore, the first objective of this study is to introduce the Phase-Weighted Relative Back Projection method (PWBP) and to verify its superiority with respect to some other BP methods.

Since the adoption of a 3-D velocity model in BP can have a positive effect, it is expected that a combination of PWBP and 3-D travel time calculation will further improve spatial resolution and deliver even better results. Thus the second goal of this study is to demonstrate the advantage of the 3-D Phase-Weighted Relative Back Projection method (3-D PWBP). We use both synthetic tests and the well-studied 1997 M_w 7.2 Zirkuh earthquake in eastern Iran to validate the new method, as its $\sim$125 km-long surface rupture and subvertical fault geometry have been unambiguously confirmed using both field and geodetic data (Berberian et al., 1999; Sudhaus & Jónsson, 2011). Then we apply the 3-D PWBP to the 13 November 2016 M_w 7.8 Kaikōura earthquake, which is known to have involved a network of at least a dozen reverse and strike-slip faults within the Marlborough Fault System of New Zealand (Hamling et al., 2017; Cesca et al., 2017; Holden et al., 2017; Wang et al., 2018). With the high resolution of our new approach, the 3-D PWBP results may provide additional insights to the detailed spatiotemporal distribution of coseismic slip in this multi-fault earthquake.

2.2 The 3-D PWBP Method

RBP differs from the conventional BP technique in its use of a reference station for determining travel time differences (Zhang & Ge, 2010). The 3-D PWBP method builds upon RBP with two additional features: phase-weighted stacking and travel time calculation with a 3-D velocity model. In this section, we first briefly describe the RBP method, and then explain in detail how we implement the two additional features.

In RBP, the source area is divided into a grid, an array of stations within the distance range of 30–90° is chosen, and theoretical travel times are calculated between each grid node and each station. The first step is to set the epicenter and reference station at grid node j_0 and station k_0, respectively. The theoretical travel time between grid node j and station k is τ_{jk}. When a subsource is located at grid node j, its signal is expected to have time delays of $(\tau_{jk} - \tau_{j_0k})$ at station k and $(\tau_{jk_0} - \tau_{j_0k_0})$ at the reference station k_0. Thus, the time shift at station k due to a subsource at j, with respect to the reference station k_0, is:

$$T_{jk} = (\tau_{jk} - \tau_{j_0k}) - (\tau_{jk_0} - \tau_{j_0k_0}) \tag{2.1}$$

Given any time t_0 at the reference station k_0, we can trace back the energy emitted at each grid node ($E_{S_j}(t_0)$) by stacking normalized seismograms recorded at each station according to the time shifts T_{jk}, and adding the squared value within the expected arrival time window, that is:

$$E_{S_j}(t_0) = \sum_{t_0-\frac{win}{2}}^{t_0+\frac{win}{2}} S_j(t)^2 \tag{2.2}$$

$$S_j(t) = \frac{1}{M}\sum_{k=1}^{M} w_k(t+T_{jk}), t \in (t_0 - \frac{win}{2}, t_0 + \frac{win}{2}) \tag{2.3}$$

where M is the number of stations, w is the seismogram, and win is the time window duration. The grid node(s) with peak energy represent the location of subevent(s). Finally, the rupture time t_r is obtained as

$$t_r = t_0 - (\tau_{jk_0} - \tau_{j_0k_0}) \tag{2.4}$$

To enhance the extraction of relevant signals from the background noise, we take advantage of the phase-weighted stacking technique (Schimmel & Paulssen, 1997). The basic premise of phase-weighted stacking is that both amplitude and phase should change synchronously in correlated signals. In other words, a coherent signal would be recognized by the phase-weighted stacking only when both the amplitude and phase are well aligned across the recording stations.

For a given seismogram $w(t)$, we use the Hilbert transform to obtain the amplitude A and phase φ as functions of time t:

$$W(t) = H(w(t)) = A(t) \cdot e^{i\varphi(t)} \tag{2.5}$$

where i is the imaginary unit.

By modifying equation 2.3 with equation 2.5, the PWBP is defined as

$$S_j(t) = [\frac{1}{M}\sum_{k=1}^{M} w_k(t+T_{jk})]^m[\frac{1}{M}\sum_{k=1}^{M} e^{i\varphi_k(t+T_{jk})})]^n \qquad (2.6)$$

in which different emphases can be given to the amplitude and phase terms by adjusting the exponents m and n, respectively. The energy of the PWBP is defined by Eq. 2.2. Using the phase as a weighting factor in the stacking process, Eq. 2.6 can enhance weak signals as long as both the amplitude and phase are coherent. In contrast, the stacking value will be small when the phases are incoherent at most stations even when the amplitudes are large. This is particularly useful in cases that a subevent with small amplitude is close to a large peak from another subsource or where there is contamination of waveform amplitude from cultural noise or other non-source effects.

The term "energy" is used in early BP papers even though the value we calculated by Eq. 2.2 or 2.3 cannot be related directly to energy due to amplitude normalization (Ishii et al., 2005, 2007). The quantity calculated by Eq. 2.2 and 2.6 is even more distantly related to the true energy released by the source because of phase weighting. However, the output value in both RBP and PWBP still provides a measure of the strength of relative seismic energy release, useful for detecting the subevent location. To avoid confusion, we use a new term "Relative Energy (RE)" to describe the quantity used for subevent identification and selection in any BP method. Thus, different BP methods have different definitions of RE (e.g. CC coefficient in CCBP (Ishii, 2011) and the solution of a second order cone problem in CS (Yao et al., 2011)).

Originally, MUSIC BP uses the MUSIC pseudo-spectrum to identify the subsource location and then use its signal power to represent the relative energy release (Meng et al., 2011). In our tests, however, we found that only using the signal power gives similar or even better resolution. Thus, RE for MUSIC BP in this study is simply defined as the MUSIC pseudo-spectrum signal power. Since none of the aforementioned RE represents true energy, it is meaningless to compare RE values among methods. Nevertheless, the subevents selected according to RE carry information with which the accuracy, uncertainty and resolution of the methods can be compared.

Theoretically, the stacked phase equals 1 if the signals are synchronized, and smaller than 1 otherwise. Larger n therefore results in a stronger effect on mitigating the artefacts without affecting synchronized signals. But in real cases, because the phase changes more rapidly than the amplitude, taking high powers (e.g., $n = 10$) in Eq. 2.6 may cause a stability issue in the result. In contrast, $n = 1$ is usually not enough to mitigate the artefacts. We did experiments with synthetic seismograms of two point sources and real Kaikōura data, both of which show significantly less scattering effect when $n = 2$, 3, 4, or 5. Meanwhile, the results are very similar with n in the range of 2 to 5. Therefore, we use $m = 1$ and $n = 3$ throughout this study, which is also consistent with Rost and Thomas (2002) and Fan and Shearer (2017).

Finally, we use a 3-D velocity model to compensate the effect caused by velocity anomalies along the propagation path which could not be corrected by alignment of the first peak. In this study we adopt the LLNL-G3-DV3 global P-wave tomography model (Simmons et al., 2012) in our travel time calculation, but we emphasize that any 3-D velocity model can be incorporated, depending on the study area dimensions and the required resolution.

Since the resolution of the LLNL-G3-DV3 model is one degree by one degree in the upper mantle and much lower beneath it, one concern is whether there is any resolvable difference between using 1-D and 3-D models when the rupture length is on the order of 100 km. In the case of 2016 Kaikōura earthquake, the time shift difference between 1-D and 3-D models (i.e., $|T_{jk}^{1D} - T_{jk}^{3D}|$) is 0.24 s on average and can be as large as 0.65 s. Given the epicenter distance of 60°–90°, this time shift difference corresponds to an average spatial shift of ∼4 km and a maximum of ∼13 km.

2.3 Validation of 3-D PWBP

We compare 3-D PWBP against existing BP methods using three tests of increasing complexity. In the first (Section 2.3.1), we use synthetic seismograms perturbed with random noise to highlight the influence of phase weighting. In the second (Section 2.3.2), we use a synthetic earthquake constructed from Kaikōura aftershock seismograms to demonstrate benefits from incorporating a 3-D velocity model. Finally (Section 2.3.3), we provide further validation of the 3-D PWBP method using a real earthquake with an independently-known, simple, sub-vertical fault geometry that provides a tight constraint on the location of seismic energy release.

2.3.1 Validation of PWBP Using Synthetic Seismograms

In the original BP stacking process, uncorrelated peaks with large amplitudes may overwhelm correlated weak signals, leading to large artefacts. Including the coherency of phase in the stacking calculation can significantly reduce this effect. In this subsection, we conduct synthetic tests to demonstrate the advantage of PWBP against time domain methods, RBP and CCBP, and frequency domain methods, MUSIC BP and CS.

We generate the first test dataset using synthetic seismograms computed for six successive subsources. The first subsource is located at the epicenter of the 2016 M_w 7.8 Kaikōura mainshock, and the other five are at epicenters of five aftershocks ($M_w > 5$) at successively north-easterly positions. We assign the six subevents the same focal depth of 22 km and the same mechanism, for which we take the Global Centroid-Moment-Tensor (GCMT) solution (Dziewoński et al., 1981; Ekström et al., 2012) of the mainshock. The delay between the initiation of each subevent is set such the overall rupture speed is 1.7 km/s with each subsource rupturing for 2 s. We choose 21 South American stations (the same as those later used in studying the mainshock (Section 2.4)) and calculate synthetic seismograms at each using *qssp* software (Gilbert & Backus, 1968; Takeuchi & Saito, 1972; R. Wang, 1997).

Fig. 2.1 shows the clean waveforms filtered in the frequency band of 0.5-2 Hz and the results from PWBP, RBP, CCBP, MUSIC BP and CS. Without noise, PWBP, RBP, MUSIC BP and CS can distinguish subsources separated by only ∼14 km (the last two subevents), while CCBP suffer visibly from smearing artefacts.

We further test the performance of each method by adding noise to the synthetic seismograms. Noise is generated based on a bounded uniform random distribution on [–1, +1], and scaled so as to provide the desired signal to noise ratio (SNR=$Power_{signal}/Power_{noise}$). And we tested different sets of random numbers for

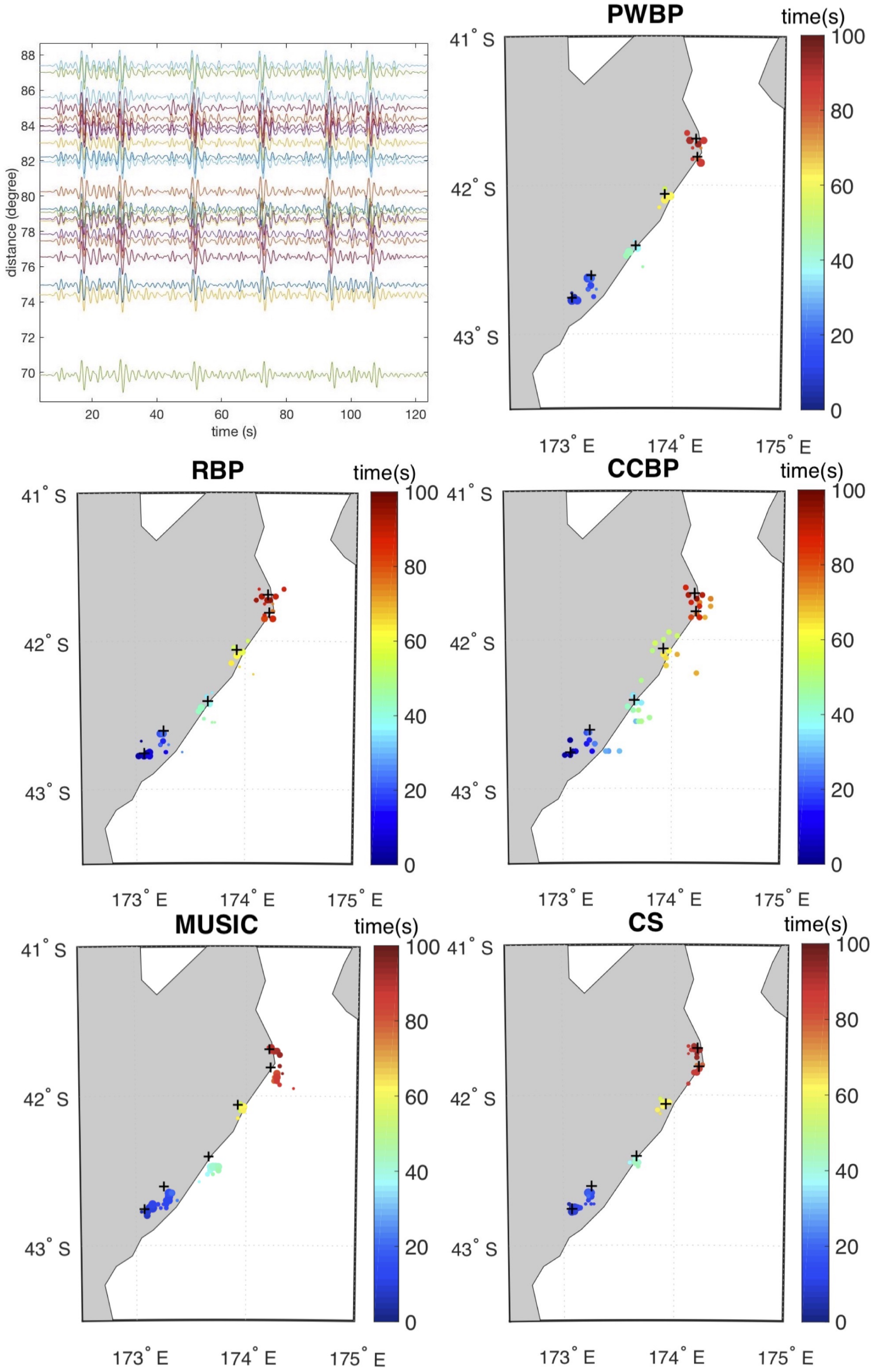

Figure 2.1: BP method comparison using synthetic seismograms without noise. Black crosses indicate locations of the six input subsources and dots showing output subsources with RE larger than 0.1 times the global maximum RE among all the steps, colored by rupture time and scaled by RE.

each SNR, which show very similar results. Therefore, we only show one representative for each SNR. Fig. 2.2 and Fig. 2.3 show waveforms with SNR = 6.4 and 3.0, respectively, and the corresponding results. When the SNR is 6.4, CCBP and MUSIC BP cannot clearly distinguish the first two subevents, whereas PWBP, RBP and CS identify them as two separate clusters, albeit with minor artefacts. However, CS mislocates the second cluster compared to PWBP. RBP fails to distinguish clearly the last two subevents, and also scatters RE more than PWBP. PWBP and CS both give two clear clusters for the last two subevents.

In the case that SNR=3.0, all five methods fail to distinguish the first two subevents which are separated by ∼22 km. CCBP clearly has more artefacts than other methods. PWBP, MUSIC BP and CS give no significant artefacts between subevents 2, 3 and 4, while RBP does. However, MUSIC BP mislocates the last two subevents by up to ∼50 km.

Overall, these synthetic tests demonstrate that PWBP and CS have the best resolution and give rise to the fewest artefacts. However, CS requires much longer calculation time (e.g., more than 10 hours in this test on a standard laptop) compared to PWBP (several minutes) and may have unstable results strongly dependent on the choice of controlling parameters. Therefore, we consider PWBP to be most advantageous among the tested methods.

In the real case, due to the imperfect velocity model and unknown noise level, the absolute resolution can differ from this synthetic test. Uncertainties arising from other factors such as variable source mechanism, source depth and instantaneous rupture directivity are also beyond the scope of this synthetic test.

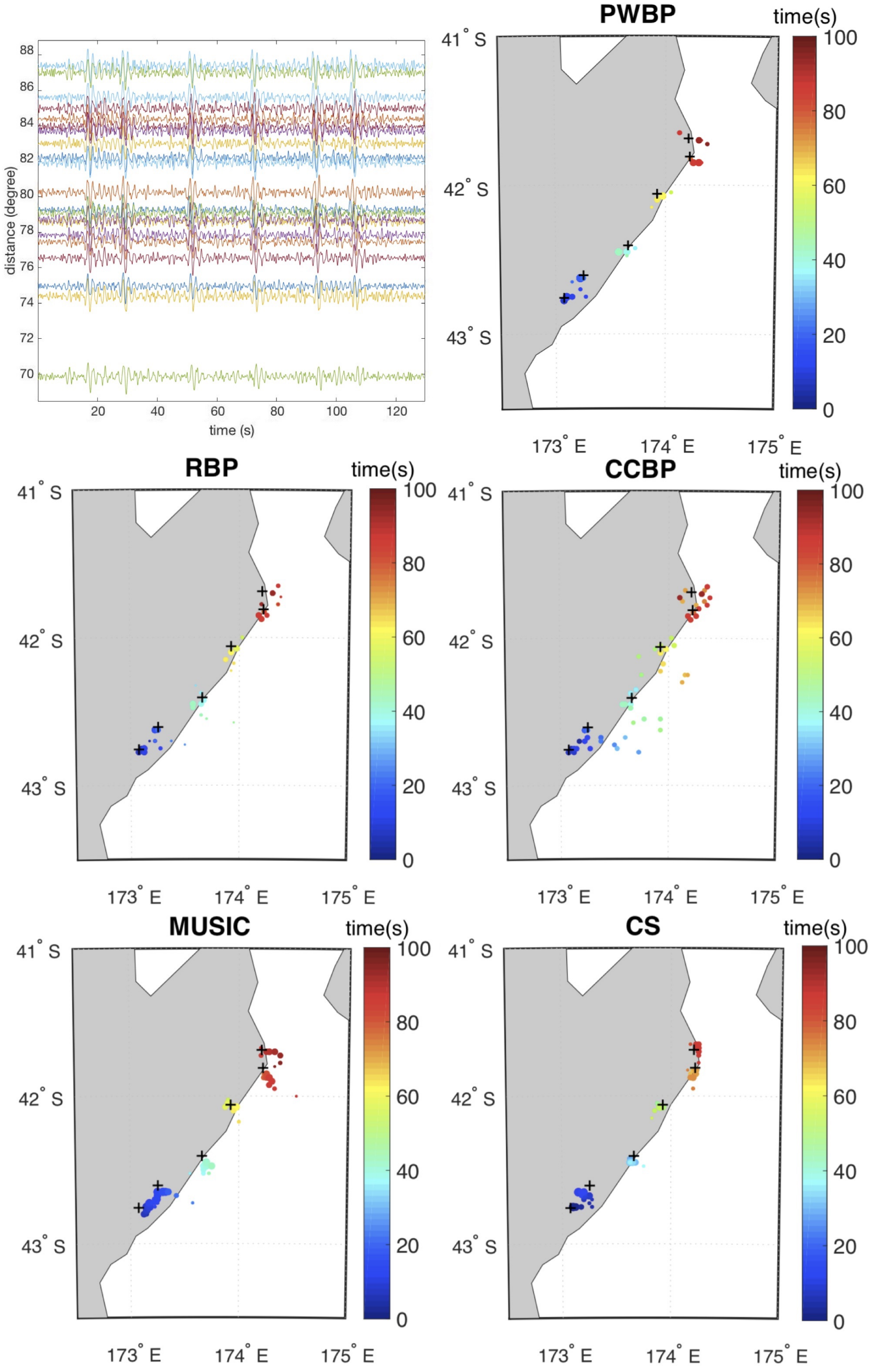

Figure 2.2: BP method comparison using synthetic seismograms perturbed with noise for a SNR of 6.4. Black crosses indicate locations of the six input subsources and dots show output subsources with RE larger than 0.1 times the global maximum RE among all the steps, colored by rupture time and scaled by RE.

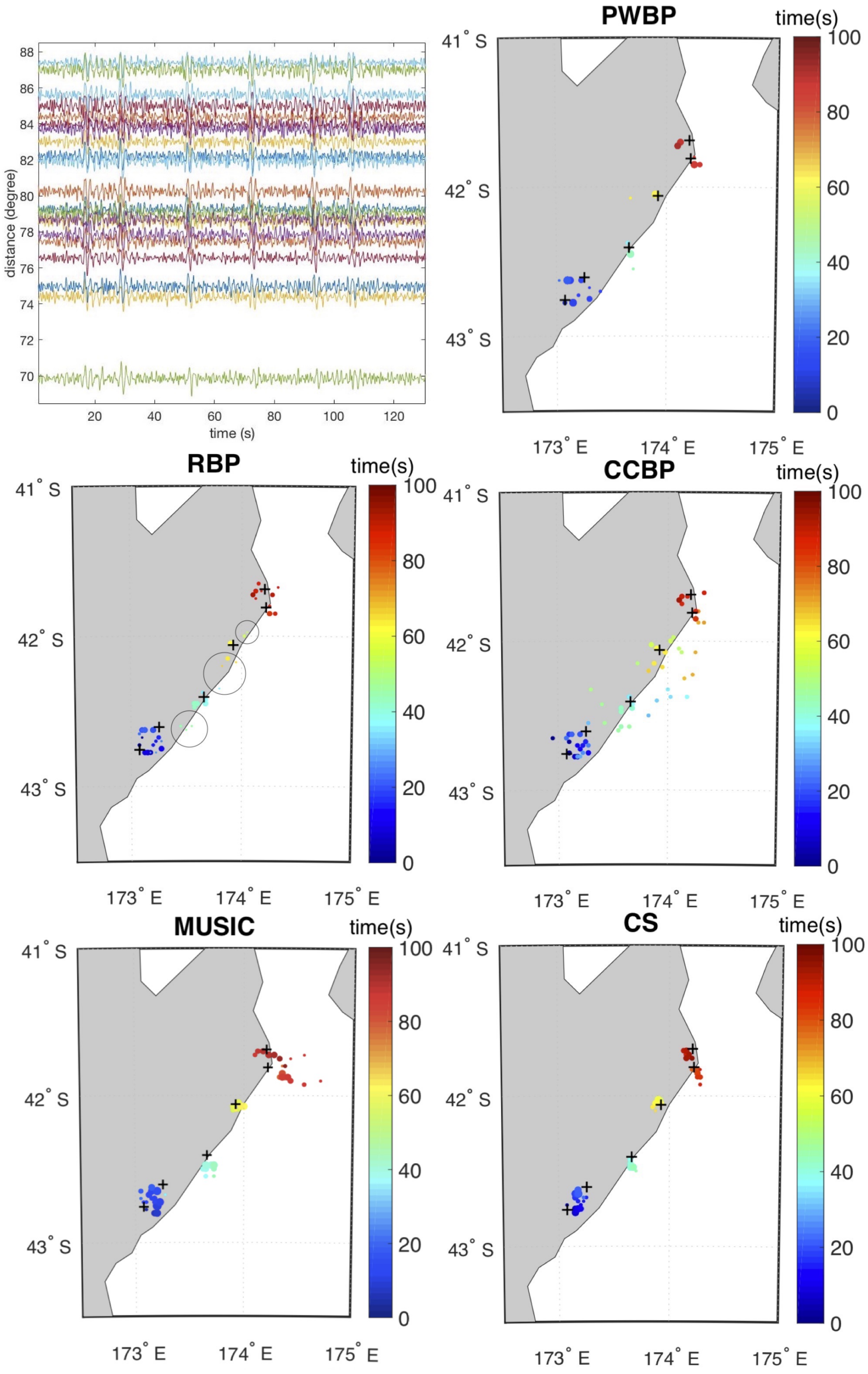

Figure 2.3: BP method comparison using synthetic seismograms perturbed with noise for a SNR of 3.0. Black crosses indicate locations of the six input subsources and dots show output subsources with RE larger than 0.1 times the global maximum RE among all the steps, colored by rupture time and scaled by RE. Black circles highlight places in which RBP gives artefacts but PWBP doesn't.

2.3.2 Validation of 3-D PWBP Using a Synthetic Earthquake Constructed from Real Aftershock Seismograms

Since Liu et al. (2017) have demonstrated that 3-D BP performs better than BP, incorporating a 3-D velocity model alongside phase weighting is expected to have a compound positive effect. To illustrate, we conduct a synthetic test in which the recorded seismograms of the 2016 Kaikōura earthquake sequence are added together to simulate the rupture of a larger, composite earthquake. This test set-up has several advantages over the fully-synthetic test used in the previous subsection. Firstly, it preserves the real travel times necessary to test the effect of the 3-D velocity model. Secondly, not only is random noise naturally built in, but the contamination of other unknown phases is also included, making the test much more realistic. Thirdly, aftershock locations, even with uncertainties, could be used as a reference to estimate the uncertainty of our own method. Finally, the absolute values of uncertainty estimated from this test could be a good proxy for the application of these methods to real earthquakes.

We construct a realistic, six-subsource model using seismograms recorded at 20 South American stations. This array is one station fewer than that used in the analysis of Kaikōura mainshock, which is presented in the next section (Fig. 2.10), due to the lack of some aftershock data at that station. The signal from the first source is generated by cutting the mainshock seismograms from 25 s before to 12.5 s after the P arrival. We similarly cut each aftershock seismogram and then splice them together, with the arrival time of each new subsource determined by its distance NE of the

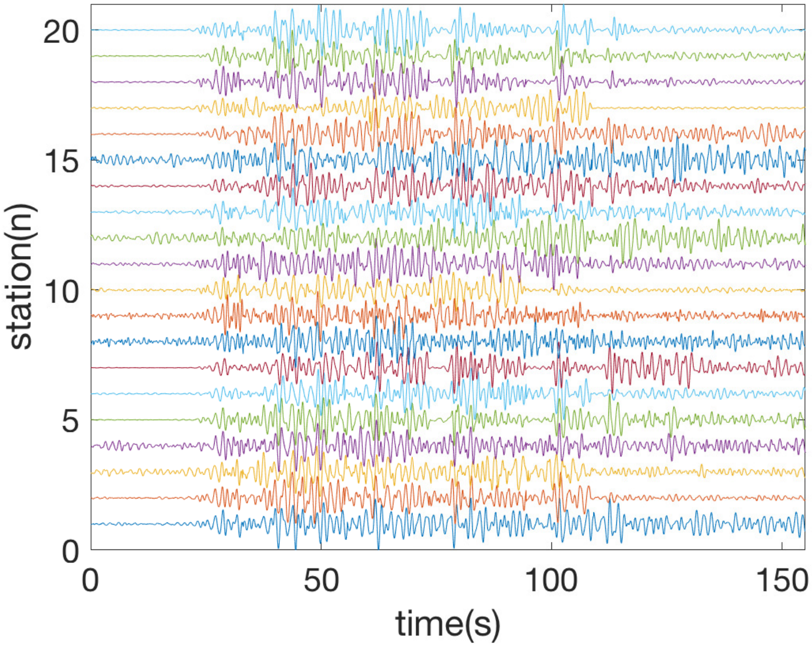

Figure 2.4: Seismograms synthesized from real seismograms of the 2016 Kaikōura mainshock and five of its aftershocks.

mainshock epicenter divided by a rupture speed of 1.7 km/s. All of the seismograms are filtered in the 0.5-2 Hz frequency band and normalized before cutting, so that the amplitudes of different events with different magnitudes are more or less equal (Fig. 2.4).

We apply four different methods (RBP, PWBP, 3-D RBP, and 3-D PWBP) to this dataset. We first determine the global maximum of the RE from all time steps. At each time step, a subevent is identified at the grid node with the maximum RE and the RE value must exceed 10% of the global maximum (Fig. 2.5). Clearly, phase weighting has a significant effect in minimizing the scattering of subsources (Fig. 2.5, RBP versus PWBP, and 3-D RBP versus 3-D PWBP). In comparison, incorporating a 3-D velocity model results in marginal benefits at some time steps but improves the overall alignment of subsources (Fig. 2.5, RBP versus 3-D RBP, and PWBP versus

3-D PWBP).

To better demonstrate the differences, we use two criteria to quantify the performance of each method. Firstly, we define the spatial resolution as the area with RE exceeding 90% of the maximum value in each time step. We acknowledge that this area may vary if a different configuration parameter is used in the stacking (e.g., the exponents m and n in Eq. 6 or the number of n-th root). However, given a reasonable range of these configuration parameters (e.g., m=1, n=3 in phase weighting and 4 in n-th root stacking), the fewer number of grid points around the maximum RE peak, the higher spatial resolution this method can achieve. Similar practice has been implemented in previous studies (e.g., Kao & Shan, 2004; Yao et al., 2011; Liao et al., 2012; Fan & Shearer, 2017).

Fig. 2.6 shows 50% and 90% RE contours at two selected time steps. Table 2.1 shows the number of grid nodes above the 90% threshold at 10-s time increments. The improvement from RBP to 3-D PWBP is defined by $\Delta_{total} = (N_1 - N_2)/N_1 \times 100\%$, where N_1 and N_2 are the numbers of grid nodes above the 90% threshold derived by RBP and 3-D PWBP, respectively. The average improvement is 95%, meaning that the area above the 90% RE threshold in 3-D PWBP is only one-twentieth of that in RBP. Meanwhile, we can also distinguish the separate effects of phase weighting and 3-D velocity structure: the average improvement due to phase weighting is ∼90% (Table 2.1, columns 1 to 3 and 2 to 4) whereas the average improvement due to the 3-D velocity model is just ∼40–60% (Table 2.1, columns 1 to 2 and 3 to 4).

It is worth noting that choosing a different threshold would lead to similar results, and in turn, similar improvements (as shown by the 50% contour lines in Fig. 2.6).

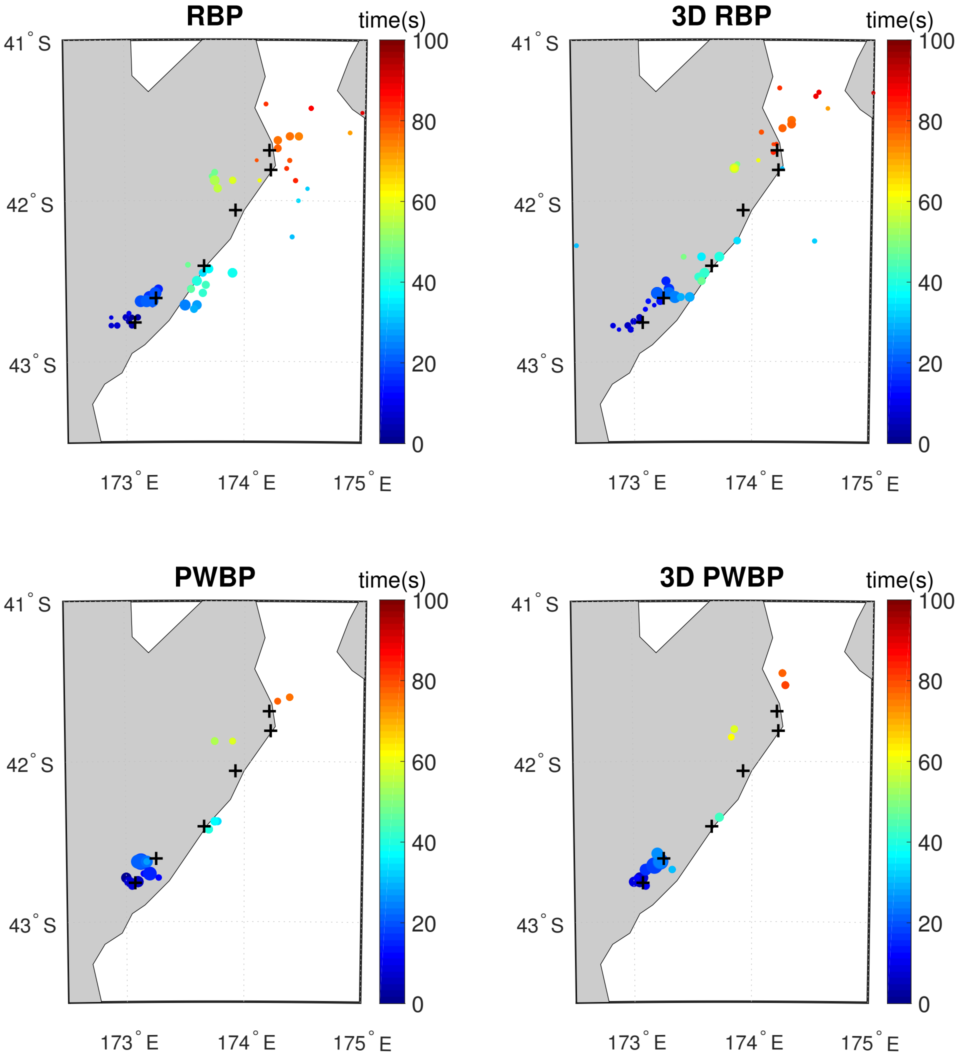

Figure 2.5: Results for the synthetic aftershock test of 3-D PWBP. Circles show obtained subevent locations colored by rupture time. Black crosses show corresponding aftershock locations (reported by the United States Geological Survey (USGS), retrieved from the Incorporated Research Institutes for Seismology (IRIS) website). The rupture times of six subevents are set to be 0 s, 12 s, 35 s, 55 s, 76 s, 88 s, respectively, from southwest to northeast.

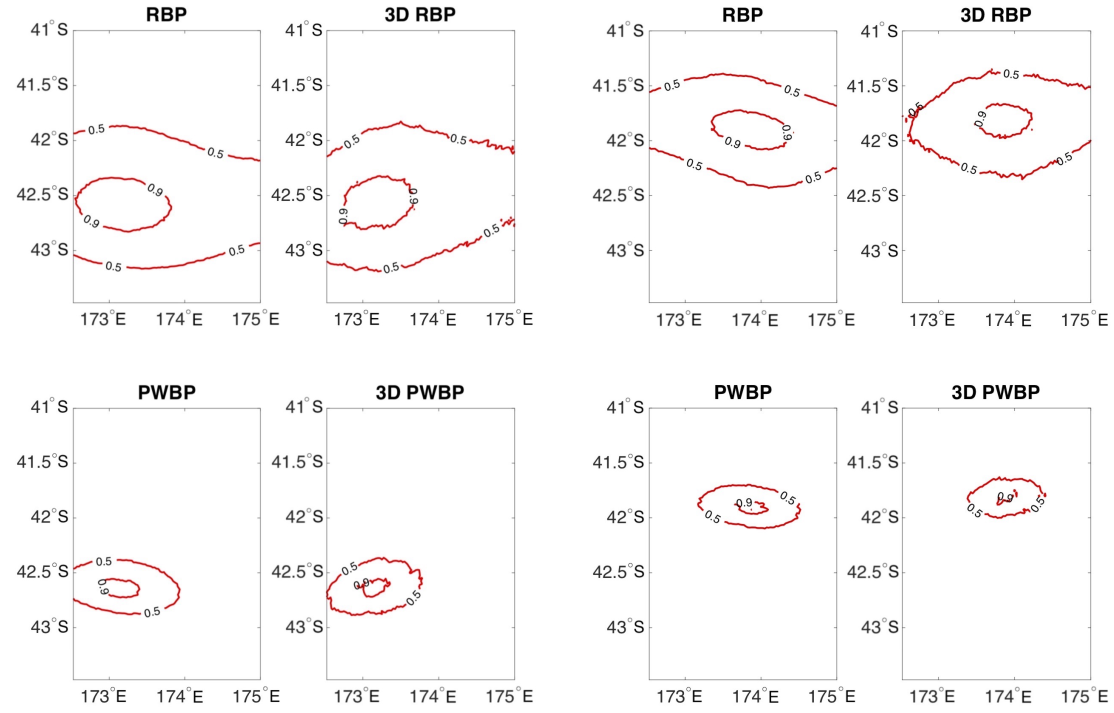
RBP
3D RBP
RBP
3D RBP
PWBP
3D PWBP
PWBP
3D PWBP

Figure 2.6: 90% and 50% RE contours in the 20^{th} step (left) and the 60^{th} step (right) of our synthetic test. RE is normalized to the peak RE in each time step.

Thus, we conclude from this test that 3-D PWBP has the highest resolution, with phase weighting playing a more important role in this improvement than incorporation of the 3-D velocity model.

The second criteria used to quantify method performance is the distribution of solutions obtained using a bootstrapping approach (Efron, 1979; Tichelaar & Ruff, 1989). Bootstrapping has been widely used in the seismological community to estimate earthquake location uncertainties from the distribution of solutions obtained using randomly subsampled input data (e.g., L. Bai et al., 2006; Jia et al., 2017). We apply the same approach to estimate uncertainties in the location of RE from different BP methods. We perform BP using 18 seismograms randomly picked from the 20

Table 2.1: Comparison of 90% RE area, represented by number of nodes within the 90% RE contour, for different methods.

Time step	RBP	3-D RBP	PWBP	3-D PWBP	Δ_{total}
10s	808	637	133	76	91%
20s	737	554	106	67	91%
30s	1183	461	85	13	99%
40s	573	456	102	16	97%
50s	362	247	24	11	97%
60s	429	261	59	22	95%
70s	548	101	9	3	99%
80s	448	294	84	43	90%

Table 2.2: Average standard deviation ($\bar{\sigma}$, km) of distances between individual subevent location and the median location in all time steps by different methods in the bootstrapping test

RE Threshold	RBP	3D RBP	PWBP	3D PWBP	Δ_{total}
0.05	33	30	26	23	29%
0.1	30	28	22	22	26%
0.2	24	21	21	21	12%

used previously (repetition allowed) to identify subsources, and repeat twenty times. At each time step and for each method, we therefore obtain 20 subevent locations whose median is drawn onto the map. We then calculate the standard deviation (σ) of distances between individual subevent location and the median location. The average (algebraic mean) standard deviation ($\bar{\sigma}$) for all time steps indicates the uncertainty of the method.

As shown in Fig. 2.7, RBP and 3-D RBP have σ up to >100 km, while those of PWBP and 3-D PWBP are <55 km. The average uncertainties ($\bar{\sigma}$) of RBP, PWBP, 3-D RBP and 3-D PWBP for a RE threshold of 0.1 are listed in Table 2.2. Following the definition outlined in the previous test, the improvement from RBP to 3-D PWBP is 26%, with improvements due to phase weighting and incorporating a 3-D velocity model of 23% and 4%, respectively.

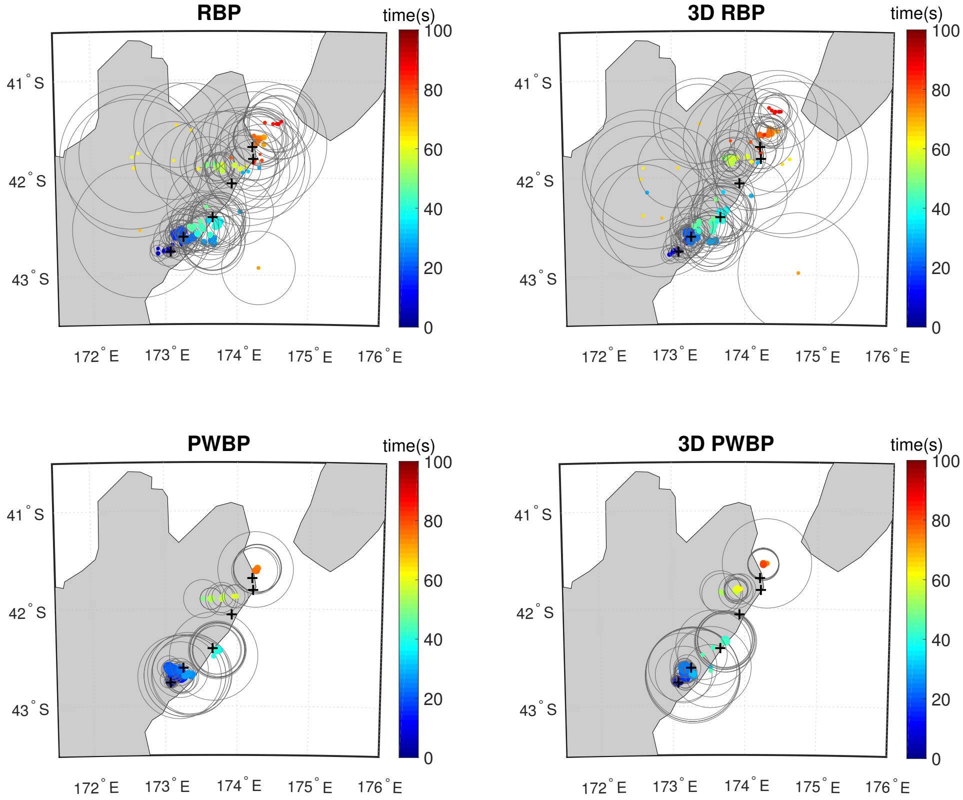

Figure 2.7: Bootstrapping test results. Black crosses show the locations of the six aftershocks. Dots represent the median location of obtained subsources at selected time steps, colored by median time and scaled by median RE. Grey circles show the standard deviations (σ) of distances between individual subevent location and the median location in each time step.

Different RE thresholds may significantly affect the spread of bootstrapped subevent locations, with lower thresholds giving rise to larger $\bar{\sigma}$ as more noisy nodes are included. In Table 2.2, we show how $\bar{\sigma}$ varies with RE thresholds of 0.05, 0.1 and 0.2. As the selection criterion becomes more restrictive, the differences among the methods gradually vanish, but 3-D PWBP always has the smallest $\bar{\sigma}$. From this test we thus conclude that 3-D PWBP gives rise to the smallest uncertainty and, similar to the test of spatial resolution, phase weighting is more influential than incorporating the LLNL 3-D velocity model. The bootstrapping result is also consistent with the previous synthetic experiment (Fig. 2.5), with both showing that 3-D PWBP produces a less scattered distribution of subsources than other tested methods.

Finally, we compare the 3-D PWBP results with the input rupture model. As shown in Fig. 2.5, results for the early part of the rupture (0–50 s) are broadly consistent with the time and location of input subsources, while results for the final part (50–85 s) deviate systematically towards north. Taking the location difference between the input and output subsources, the spatial uncertainty is estimated as $\sim$10 km for the area south of 42.3° S but $\sim$20–30 km north of it. These two estimates are consistent with the $\bar{\sigma}$ of $\sim$22 km derived from the uncertainty test, providing a reference for interpreting the following 3-D PWBP analysis of 2016 Kaikōura mainshock rupture (Section 2.4). The rupture model derived by 3-D PWBP has a total duration of $\sim$85 s compared to an input duration of 88 s. The resulting uncertainty in rupture duration of $\sim$3 s can also be used for reference in the subsequent study of the Kaikōura earthquake

2.3.3 Validation of 3-D PWBP Using the 1997 Zirkuh Earthquake

Next, we compare the relative accuracy of these methods using real data from the 1997 M_w 7.2 Zirkuh, Iran earthquake, a well-studied right-lateral strike-slip event with a clear surface rupture (Berberian et al., 1999) and a complementary InSAR-derived slip model (Sudhaus & Jónsson, 2011). This particular event is selected for a number of reasons. Firstly, it created unambiguous surface ruptures over a distance of ∼125 km with its epicenter close to the northern end of the surface rupture, implying a simple unilateral rupture directivity that was confirmed with body-waveform modelling (Berberian et al., 1999). Secondly, InSAR modelling (Sudhaus & Jónsson, 2011) indicates that most seismic slip occurred over a depth range of 0–20 km on subvertical faults; thus the surface ruptures are good proxy for the location of seismic energy. Thirdly, mainshock seismic and geodetic moments are in close agreement and there were no large aftershocks, removing any doubt that the mapped surface faulting ruptured coseismically in the mainshock. Therefore, we can determine the most accurate method of imaging the rupture as the one that fits the observed surface faulting best.

To retrieve the Zirkuh rupture process we used 21 stations in and around Europe (Fig. 2.8), filtered the seismograms in the 0.15–2 Hz frequency band (Fig. 2.8), and applied a 12 s sliding window with 1 s time step. These data were processed using the four BP variants under consideration: RBP, PWBP, 3-D RBP and 3-D PWBP. Final subevents are selected by applying different RE thresholds, namely, 0.05, 0.1 and 0.2 times the global maximum among all the time steps, respectively. This selection is

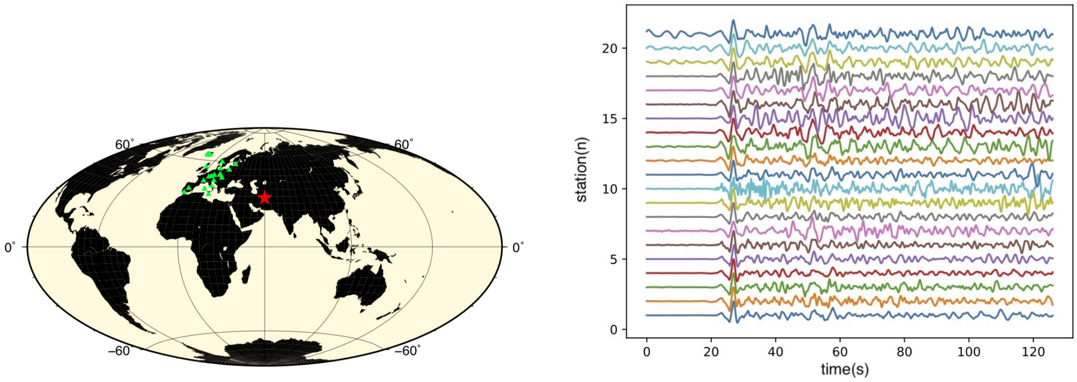

Figure 2.8: Left: locations of the 1997 Zirkuh, Iran earthquake epicenter (red star) and the BP array (green triangles). Right: selected seismograms of the 1997 Zirkuh earthquake, aligned and filtered by the 0.15–2 Hz band, and plotted at equal spacing.

necessary but the threshold is not critical because scattered solutions with very small RE occur in some time steps which are obvious artefacts and could be ruled out by any aforementioned threshold. Therefore, we show the results and comparison with threshold of 0.1 in detail first (Fig. 2.9), followed by a discussion about different thresholds.

RBP and 3-D RBP methods both give rise to large artefacts SE of the surface rupture terminus (black ellipses in Fig. 2.9a, 2.9b), and adding in the phase weighting reduces or eliminates these artefacts (Fig. 2.9c, 2.9d). Incorporating a 3-D velocity model concentrates BP energy closer to the observed rupture, particularly in the southeast (see dashed lines on Fig. 2.9a versus 2.9b, and Fig. 2.9c versus 2.9d). Thus, 3-D PWBP, in combining phase weighting and 3-D velocity structure, maximizes the benefits of both approaches. In our preferred 3-D PWBP model, we estimate a rupture duration of ∼35 s and an average rupture velocity of ∼3.0 km/s

We measure the distance between each subsource and the nearest fault trace,

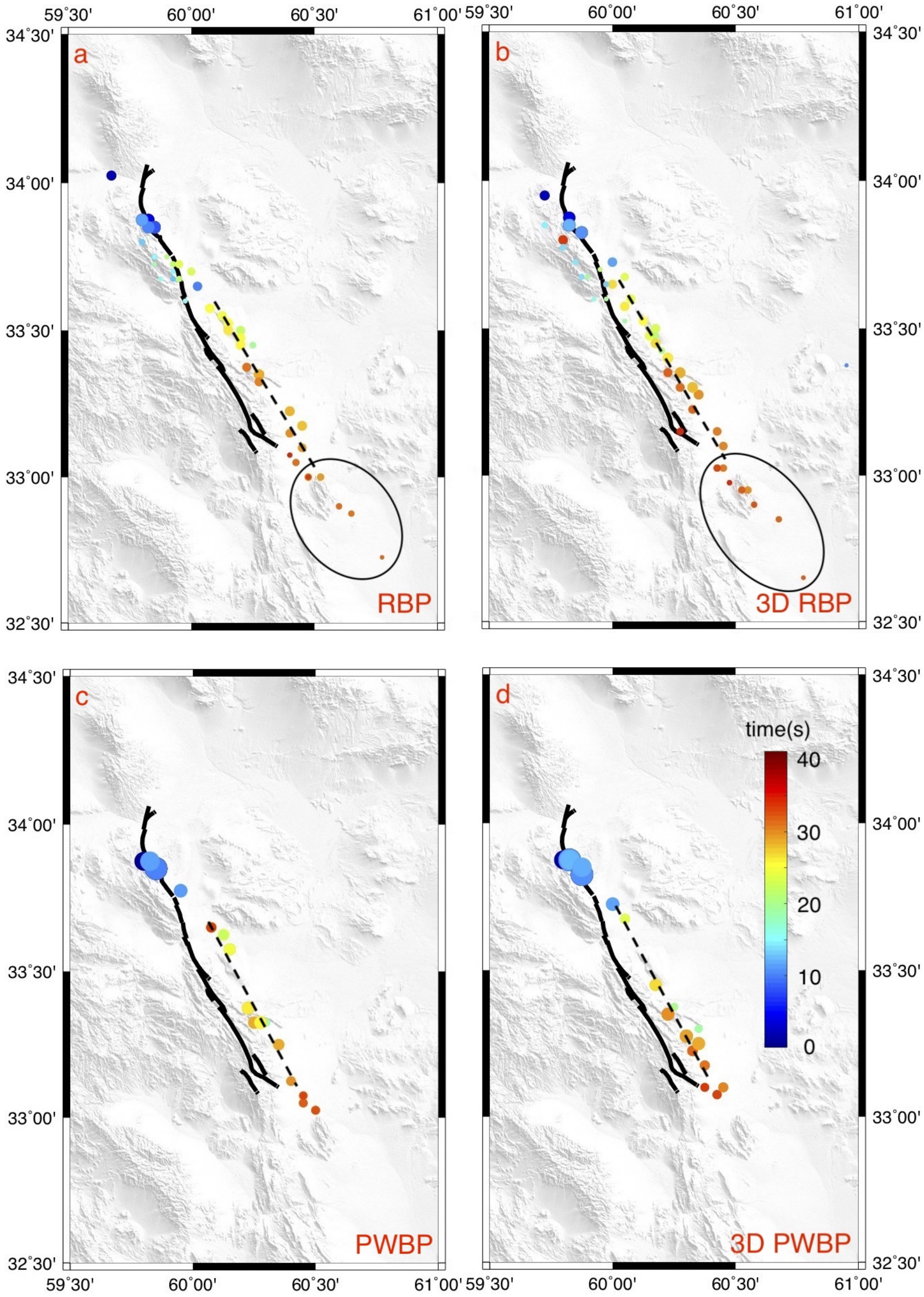

Figure 2.9: Rupture process of the 1997 Zirkuh earthquake from (a) RBP, (b) 3-D RBP, (c) PWBP and (d) 3-D PWBP. Solid black lines are surface ruptures (Berberian et al., 1999). Dots represent the obtained subevents, colored by rupture time and scaled by RE. Black ellipses highlight artefacts in the non-phase-weighted solutions SE of the surface rupture termination. The dashed line shows the energy trend along the SE half of the fault, which consistently lies NE of the mapped surface rupture, but is closer to it when the 3-D velocity structure is implemented.

Table 2.3: Mean (μ, km) and standard deviation (σ, km) of the distance between imaged subsources and surface rupture trace of the 1997 Zirkuh earthquake for different methods.

RE Threshold	Indicator	RBP	3D RBP	PWBP	3D PWBP	Δ Total
0.05	μ	8.6	8.7	8.1	4.9	43%
	σ	9.7	11.4	5.1	3.8	60%
0.1	μ	8.6	8.6	8.6	4.8	45%
	σ	9.8	11.4	5.2	3.9	60%
0.2	μ	8.6	7.6	7.4	4.2	51%
	σ	7.8	7.4	5.0	3.7	52%

then calculate the average (μ) and the standard deviation (σ) of all residual distances as indicators of model fitness (Table 2.3, RE Threshold=0.1). The mean residual distance remains unchanged when the RBP, PWBP or 3-D RBP methods are used, but decreases by ~45% in the case of using 3-D PWBP. The standard deviation increases slightly from RBP to 3-D RBP, but drops dramatically from RBP to PWBP. When both phase weighting and 3-D velocity model are incorporated (3-D PWBP), it improves by as much as ~60%. It is no surprise that using the 3-D velocity model with the conventional RBP method does not improve the σ value, since results include many artefacts and become even more scattered when the 3-D velocity model pulls the imaged rupture closer to the fault trace. In contrast, phase weighting mitigates artefacts but does not map the BP energy closer to the fault. It is only by combining phase weighting and the 3-D velocity model that we see an obvious improvement in subsource locations. This conclusion is consistent with Fan and Shearer (2017) that PWBP alone does not improve the location accuracy of imaged events.

Finally, we investigate the effect of varying the RE threshold used in selecting subsources, similar to the bootstrapping test described in the previous section. As shown in Table 2.3, we find little change when the RE threshold is set to 0.05, 0.1 or 0.2, and the total improvement from RBP to 3-D PWBP remains at the level of 40–50% (i.e., ~4 km). This distance is very close to the average spatial shift between the 1-D and 3-D velocity models (Section 2.2). In all cases, the benefit of incorporating the 3-D velocity model becomes obvious only when phase weighting is applied. We thus conclude that the improvement in the location of subsources is mainly due to the choice of method rather than the selection of RE threshold, and that 3-D PWBP gives the most accurate results among the tested methods.

2.4 Application to the 2016 M_w 7.8 Kaikōura earthquake

The Kaikōura earthquake involved a complex rupture process that incorporated slip on more than a dozen distinct faults (Clark et al., 2017; Hamling et al., 2017; Kaiser et al., 2017; Litchfield et al., 2018). Application of several other back projection techniques either lacked the resolution to image this complexity (Hollingsworth et al., 2017), or included significant energy release at large (>40 km) distances or systematic deviations from the eventual mapped faults (Zhang et al., 2017; Kaiser et al., 2017; Liu et al., 2018; D. Wang et al., 2018). In this section, we apply the higher-resolution 3-D PWBP to this earthquake, with the goal of providing additional insight to the complex rupture path.

Given the epicenter location, only an Asian-Australian or South American array meets the BP requirements, but the former covers too large an area, weakening the correlation among traces. In contrast, stations in South America are distributed

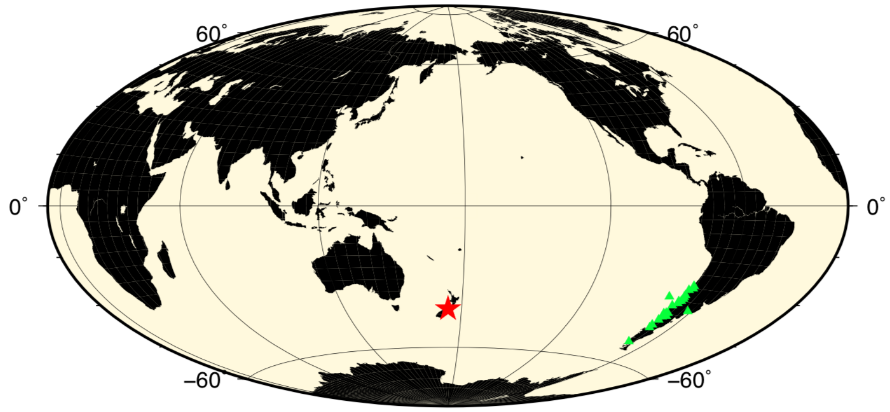

Figure 2.10: Locations of the 2016 M_w 7.8 Kaikōura, New Zealand earthquake epicenter (red star) and the selected stations in south America array (green triangles).

nearly linearly in the N–S direction, and so retain a large enough azimuth range. For this reason, we choose vertical component seismograms from 72 South American stations for this application (Fig. 2.10). Station "GO06", located in the approximate array center with SNR$\approx 3 \times 10^2$, is selected as the reference station j_0. We align the seismograms by cross-correlating a time window spanning from 4 s before to 4 s after the P wave arrival, and remove records with low coefficients. Clusters of seismic stations are thinned in order to obtain a roughly uniform station density across the array. We finally pick out 21 records with CC coefficients of $\geq$0.88 and filter them with a 0.5–2 Hz band-pass filter, before deploying 3-D PWBP. We use an 8 s sliding window to map the RE at each 1 s time step for a total of 150 s. We take the grid node with the maximum RE as the subevent location, but to account for the earthquake complexity we also allow up to three subevents with values larger than 70% of peak energy in any single step.

The final rupture process is obtained by filtering out 3-D PWBP subevents with RE below 10% of the global maximum value of all time steps (Fig. 2.11a). The main shock rupture lasts ∼84 s and comprises two major stages (before ∼46 s, and after ∼54 s), and possibly a few minor ones (Fig. 2.12). During the first major stage, the rupture remains close to the epicenter for ∼10 s, before migrating northeastwards along the Humps fault up to a time of ∼25 s. It then jumps onto the Hundalee fault, migrating northeastwards up to ∼46 s, when this first main stage abruptly stops. We observe no clear energy release between ∼46 s and ∼54 s, when the second main stage of the rupture initiates ∼30–40 km to the north.

The mapped rupture in the second main stage does not align with the surface rupturing faults as closely as that in the first stage, but still falls within our estimated uncertainty of ∼20–30 km (Section 2.3.2). It starts ∼20 km NW (but within error) of the Jordan fault. At ∼73 s, we observe some energy offshore, east of the Papatea fault. Finally, starting at ∼74 s, we observe energy ∼20 km N of the Kekerengu fault before the rupture stops abruptly at ∼84 s. Overall, the second main stage releases more energy despite its shorter duration. The rupture speeds for the two main stages are ∼1.6 km/s and ∼1.3 km/s, respectively, and the average end-to-end speed for the whole rupture is ∼1.7 km/s.

Next, we compare our final results with a published BP study by Zhang et al. (2017), which utilized a similar South American array. Using RBP, they imaged large lineations that extend up to ∼70 km NW of the mapped faults at ∼0–20 s, ∼30–40 s and ∼60–70 s, which we consider to be artefacts (Fig. 2.11b). Consequently, we consider the large offshore subevent at ∼95 s to be questionable, even though it is close to the mapped Needles fault, which was inferred to have ruptured coseismically from measurements of nearby coastal uplift (Clark et al., 2017). The first 60 s of

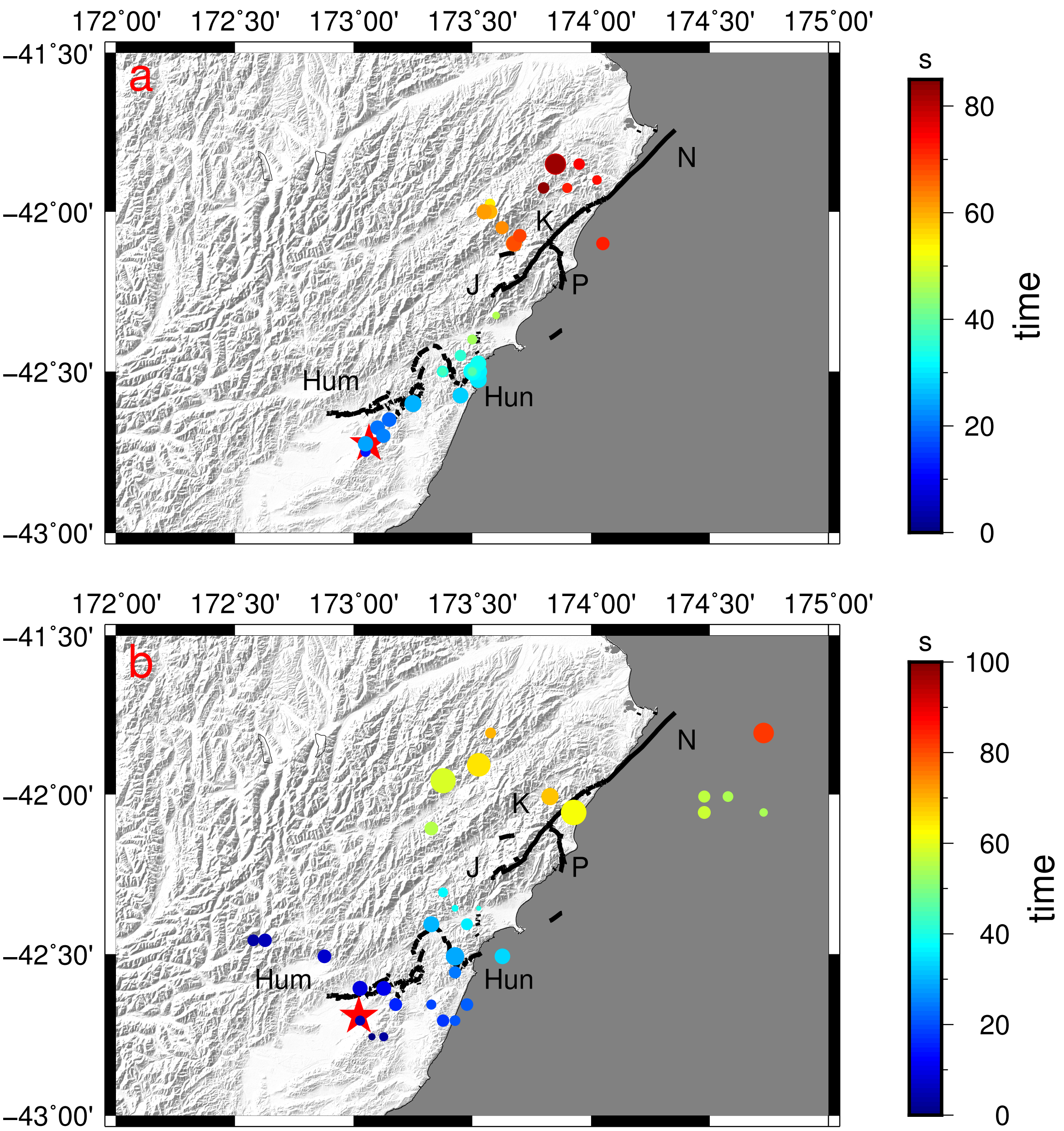

Figure 2.11: (a) Final rupture process of 2016 Kaikōura (New Zealand) earthquake, derived from 3-D PWBP and after filtering small RE. Circles show subevents scaled by RE and colored by time. The red star shows the epicenter (retrieved from IRIS website, reported by USGS). Letters are abbreviations of fault names (Hum: Humps, Hun: Hundalee, J: Jordan, P: Papatea, K: Kekerengu, N: Needles.). (b) The rupture process derived by Zhang et al. (2017) using RBP with South American data.

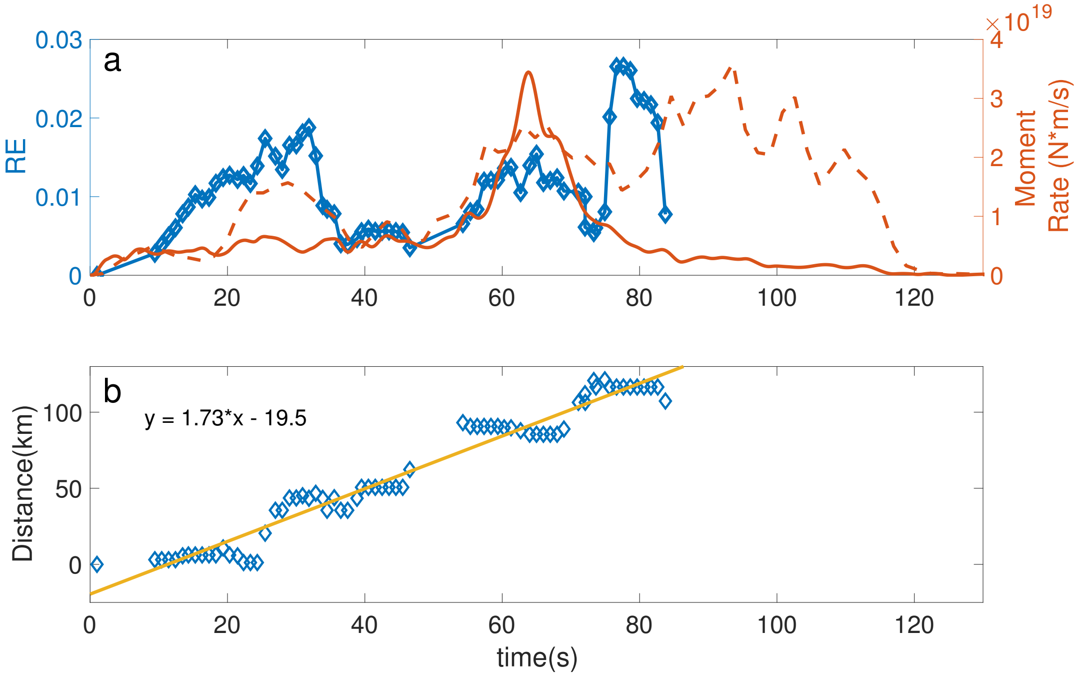

Figure 2.12: (a) The blue curve shows RE release as a function of time for our final 3-D PWBP model of the 2016 M_w 7.8 2016 Kaikōura, New Zealand earthquake, with blue diamonds indicating each discrete data point. The red solid line and dashed lines show moment release rates from Wang et al. (2018) and Wen et al. (2018), respectively. (b) Subevent distance from the epicenter as a function of time in 3-D PWBP results. The average rupture speed is 1.73 km/s, marked by the yellow line derived by linear fitting.

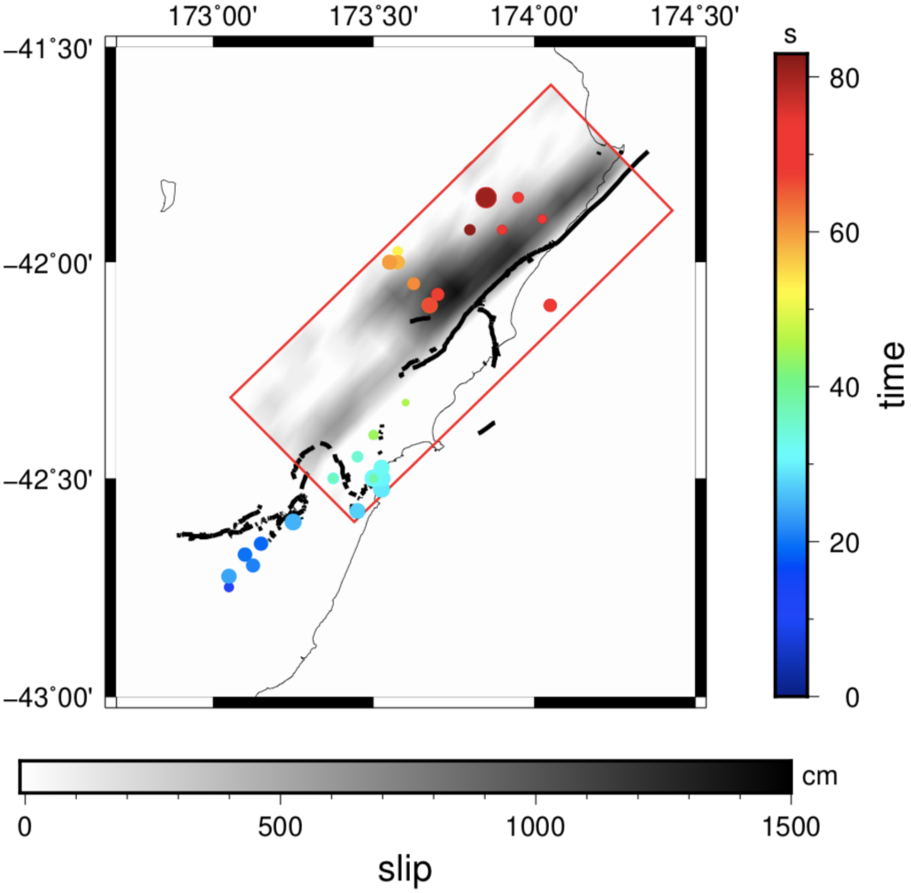

Figure 2.13: Final 2016 Kaikōura earthquake rupture process results overlaid on model of coseismic slip on the subduction zone interface from Wang et al. (2018) (red rectangle and colored slip distribution). The surface rupture and coastline are the same as for Fig. 2.11.

our rupture model is compatible with an earlier BP study by D. Wang et al. (2018) using data from an alternative Australian/SE Asian array. After 60 s, the main energy release in D. Wang et al. (2018)'s model starts on the southern segment of the Jordan Thrust and extends westwards, in the opposite direction of the observed surface rupture trend. Their results also have a larger uncertainty of ∼40 km for areas north of 42.5°N and a longer total rupture duration of >90 s.

Our total rupture duration of ∼84 s is in better agreement with several joint moment tensor models (Hollingsworth et al., 2017; Duputel & Rivera, 2017; Wang et al., 2018) and joint finite fault models (Wang et al., 2018; Cesca et al., 2017; Holden et al., 2017), all of which show major moment release terminating at around 80–90 s. Considering possible uncertainties of ∼20–30 km in the northern part of the source area, confidently ascribing any subevents to the Needles fault is challenging, but neither we nor D. Wang et al. (2018) find clear evidence of high frequency energy on this fault. We tentatively interpret that rupture along the Needles fault (Clark et al., 2017) was caused instead by a cluster of M ∼5 aftershocks that align in this area (Hamling et al., 2017; Cesca et al., 2017), by low-frequency seismic energy that is poorly-resolved by BP, or by postseismic afterslip.

Our observed variation of RE as a function of time also correlates well with the moment rate function (source time function) of published joint finite fault models. We acknowledge that RE is not a physical quantity directly derived from slip, moment rate or seismic energy, though, it characterizes peaks of high frequency energy release in both space and time domains. Therefore, the two functions should have a similar trend if they are associated with the same rupture characteristics. Since different finite fault models share some common features in their moment rate functions, we take Wang et al. (2018) and Wen et al. (2018) as two representative examples for comparison (Fig. 2.12a). Wen et al. (2018) identify 3 major peaks at ∼30 s, ∼45 s, and ∼65 s, which correspond well with our RE function. However, the rupture in their model terminates at ∼120 s, significantly later than most other models. The model by Wang et al. (2018), on the other hand, shows the biggest peak around 60–70 s with diminished moment rate after 80 s. In contrast, RE peaks at ∼80 s in our 3-D PWBP, is likely a high-frequency stopping phase detectable only by BP methods (Meng, Ampuero, Sladen, & Rendon, 2012; Yao et al., 2011).

Our final 3-D PWBP subevent locations correspond well with faulting mapped or modeled in many other studies. The first stage agrees with the fault geometry and ground deformation derived from satellite and GPS data (Morishita et al., 2017; Wang et al., 2018). To the NW of the Kekerengu fault, the two subevent clusters at ∼60–70 s and ∼70–83 s match the location of slip on the subduction fault as determined by Wang et al. (2018) (Fig. 2.13). In the 2011 Tohoku-Oki earthquake, higher frequency energy was preferentially generated by the lower part of the subduction zone rupture area (Yao et al., 2011). Thus, the deviation from surface ruptures of the second main stage may reflect high frequency energy from the subduction fault. However, given the estimated uncertainties of 20–30 km we cannot rule out the possibility that they represent slip on the Jordan, Papatea or Kekerengu faults. The energy imaged offshore at ∼73 s could also be seismic slip on the subduction interface, that would be poorly imaged by geodesy, and which may have contributed toward the generation of a local tsunami (Y. Bai et al., 2017; Clark et al., 2017).

2.5 Discussion

It has been well recognized that simple linear stacking is not the optimal scheme to extract relatively weak signals, mainly due to the dominant effect of waveforms with extremely large amplitudes (Xu et al., 2009; Ishii, 2011). There are several different nonlinear stacking techniques proposed in the literature that address this issue by trying to find a balance between signal strength and signal coherence. One strategy is to directly modify the waveform amplitude by taking its n-th root (Xu et al., 2009). The other strategy is to assign different weighting factors to the waveforms to manifest coherent signals. The weighting factor can be either the CC coefficient, the semblance coefficient (Neidell & Taner, 1971; Vallée et al., 2008), or the corresponding phase (Schimmel & Paulssen, 1997, Wang et al., 2017, and this study). The methods adopting weighted stacking may appear to be very similar, but their effectiveness can vary significantly because they emphasize different physical quantities. In this study, besides CCBP (Section 2.3.1), we also tried CC-weighted BP. The results, as CCBP, show no clear improvement from RBP, suggesting that using CC as the measurements of signal coherence in BP may not be as effective as PWBP.

We have shown how incorporating phase weighting and 3-D velocity structure can improve back projection results. However, there is a large computational cost to calculating travel times with a 3-D velocity model (10 hours on a standard laptop computer for just 21 stations), and these calculations are performed using different software than BP. In contrast, RBP and PWBP have no equivalent delay as travel times are calculated in advance, and the phase weighting calculation can be performed easily as a few additional steps in a BP code. Moreover, the improvement by phase-weighted stacking is significant while the 3-D velocity model (in this study, the LLNL model) provides a more limited improvement in source location accuracy (∼4–13 km) compared to the large uncertainties (∼20–30 km), probably due to the complex structure underneath. Consequently, it is impossible to fully distinguish all the faults in Kaikōura earthquake even with the 3-D PWBP. Thus, we recommend PWBP as the best candidate to image the rupture process of a significant earthquake immediately after its occurrence, especially for matters of urgency such as rapid response or emergency management. On the other hand, 3-D PWBP is more suitable for tasks without a tight time constraint. We expect that earthquakes in areas where the velocity structure deviates most from the global average — like subduction zones — will benefit most from using a 3-D velocity model and we envisage that finer, higher quality models will further improve the resolution of 3-D PWBP in the future.

Though 3-D PWBP improves upon previous approaches, we show that the location errors of individual subevents can exceed ∼20 km. The spatial resolution is related to several factors, including the azimuth between the rupture propagation direction and the array, the array aperture, the SNR of recorded waveforms, and the frequency band used in the analysis. Normally, larger apertures increase data resolution, as long as signals from different stations are still correlated. Higher frequency waves can provide finer details of the rupture, while smoother lower frequency waves give rise to more swimming artefacts (a series of artefacts lining up in the source-array direction) and, accordingly, less improvements in our test. Hence, low frequency waves are rarely used by time domain BP methods. However, the high frequency results may be incomplete due to possible variations in the frequency content of the source process (Yao et al., 2011; D. Wang et al., 2018). For a fixed aperture, an array located in the forward rupture propagation direction may give higher spatial resolution than the one in the opposite azimuth, because of the Doppler shift in frequency content. In general, an array with the azimuth perpendicular to the rupture propagation direction is likely to give better spatial resolution because it maximizes the time difference between stations for different grid nodes. The source mechanism is also important, since if the array lies close to a nodal plane, the final results will suffer from low SNR.

For temporal resolution, the time window duration is vital. Shorter windows distinguish the source time function better but can give rise to artefacts. Empirically, we recommend that the minimum time window should be six seconds or 1.5 times of the longest period used in the data processing, whichever is larger. This allows for possible misalignment of predicted travel times due to the imperfect velocity model, and ensures a sufficient number of samples in the BP energy calculation (Eq. 2.2 and 2.3). We find that the total rupture duration is usually well resolved by 3-D PWBP. This in turn provides important constraints on the length and speed of the rupture and can even help distinguish coseismic from post-seismic rupture, as we propose for the Needles fault in the Kaikōura earthquake.

Chapter 3 The S-SNAP

3.1 Introduction

Earthquake detection and location is one of the most fundamental tasks in seismology. Detailed understanding of the spatiotemporal distribution of seismicity is critical to the success of many research efforts in seismology and geophysics. A good algorithm for earthquake detection and location should be accurate, comprehensive and efficient; ideally, the process should be entirely automatic without human intervention.

Traditional earthquake location methods determine the best solution by minimizing travel time residuals at multiple stations. It is often an iterative, linearized process along the spatial and temporal gradients of the theoretical travel time predicted with an average velocity model (e.g., J. P. Eaton, 1970; Lee & Lahr, 1975; Herrmann, 1979). Although this strategy is computationally efficient, its accuracy depends largely on two factors. First, the phase-picking must be done with caution to prevent mapping phase reading errors to hypocentral mislocation. Secondly, a velocity model that closely approximates true velocities in the subsurface is required to provide the travel time table and its gradients. It sometimes leads to a local rather than the global minimum when the first guess is far from the real hypocenter.

Grid-search-based methods, such as the QUAKE3D (Nelson & Vidale, 1990) and the NonLinLoc (Lomax et al., 2000), have been developed to ensure that the best solution corresponds to the global minimum of travel time residuals. Using 3-D velocity models in the calculation of theoretical travel times can also reduce errors due to structural heterogeneities (e.g., Nelson & Vidale, 1990; Wittlinger G. et al., 1993). Unfortunately, methods that directly depend on travel time residuals all suffer from three factors: sensitivity to inaccurate velocity model, false phase picks, and trade-offs between the event's location and origin time.

Using a totally different approach, Zhou (1994) developed the Master Station (MS) method that relies on travel time differences between a given master station and the rest of the seismic network to define the equal differential time (EDT) surfaces. The location where the greatest number of EDT surfaces intersect is deemed the hypocenter. This method successfully avoids the trade-off problem because it does not determine the original time and the hypocenter at the same time. It was further improved by Font et al. (2004) by establishing EDT surfaces for all possible station pairs. The improved method, named the Maximum Intersection (MAXI) method, can achieve high accuracy despite the presence of false picks and imperfect velocity model.

All aforementioned location methods depend on phase picking that is usually performed by analysts through visual inspection. However, manual phase-picking inevitably suffers from human errors and/or biases, and its capacity is limited by available time and resources. The capacity issue is especially prominent in the studies of aftershock sequences of major earthquakes or induced seismicity during hydraulic fracturing, when hundreds of events may occur within hours (D. W. Eaton, 2018). To address this situation, automatic techniques have been developed to perform phase-picking based on characteristic functions such as the short-term-average and long-term-average ratio (STA/LTA) (e.g., Allen, 1978, 1982; Baer & Kradolfer, 1987; Akram & Eaton, 2016) or kurtosis (e.g., Küperkoch et al., 2010; Baillard et al., 2014). In general, a kurtosis-based approach performs better than STA/LTA, but can still miss a significant number of picks compared to manual picking (e.g., $\sim 30\%$ in Baillard et al. (2014)). A different strategy is to use neural networks to mimic the human process (e.g., Dai & MacBeth, 1997; J. Wang & Teng, 1997; Perol et al., 2018). The most recently developed convolutional neural network is capable of identifying all events picked by visual inspection; however, it still gives some false alarms, and the event location accuracy is sometimes unsatisfactory (Perol et al., 2018; Ross et al., 2018). Moreover, it requires a good training dataset which is not always available.

Another line of automatic location methods was developed in the past two decades that requires no phase-picking at all, including the Source-Scanning Algorithm (SSA) and its variants (Kao & Shan, 2004; Liao et al., 2012) and the waveform cross-correlation-based template matching method (e.g., Bostock M. G. et al., 2012). The SSA searches possible events in all time and space, and is ideal for difficult situations when phase identification and association become ambiguous. It uses stacked array energy as the identifier of events, and thus always gives the solution as a 3-D volume rather than localized point source. It also has a trade-off issue between the sensitivity of event detection and the likelihood of false alarms. In comparison, template-matching techniques require similarity between seismogram pairs, and are therefore most powerful for detecting repeated events. Perol et al. (2018) show that template-matching methods can miss $\sim$20% of events compared to the manually produced catalogue.

In this study, we propose a novel algorithm that is capable of delineating extremely complicated spatiotemporal distributions of seismicity. This innovative method, named Seismicity-Scanning based on Navigated Automatic Phase-picking (S-SNAP), takes a cocktail approach that combines the advantages of three processes to automatically and comprehensively locate all seismic sources in a pre-defined model space with high accuracy and efficiency. We apply S-SNAP to a dataset recorded by a dense local seismic array during a hydraulic fracturing operation to test this novel approach and to demonstrate the superiority of S-SNAP over conventional methods.

3.2 Method

S-SNAP consists of four major processes (Fig. 3.1). The first one, preliminary source scanning, is adopted from the Improved Source Scanning Algorithm (Liao et al., 2012) which searches for seismic sources by considering every possible location and time combination. Results of the preliminary source scanning are then used next to navigate the process of P and S phase-picking within a confined segment of seismogram. The second process, phase-picking, is a simplified version of the kurtosis-based P- and S-phase picker (Baillard et al., 2014), which determines the precise onset time within the specified seismogram segment. The precisely determined P and S arrival times are used in the third process to locate earthquakes using an improved MAXI method (Font et al., 2004), which achieves high accuracy and reliability by allowing tolerances to some false picks and an imperfect velocity model. In the final process,

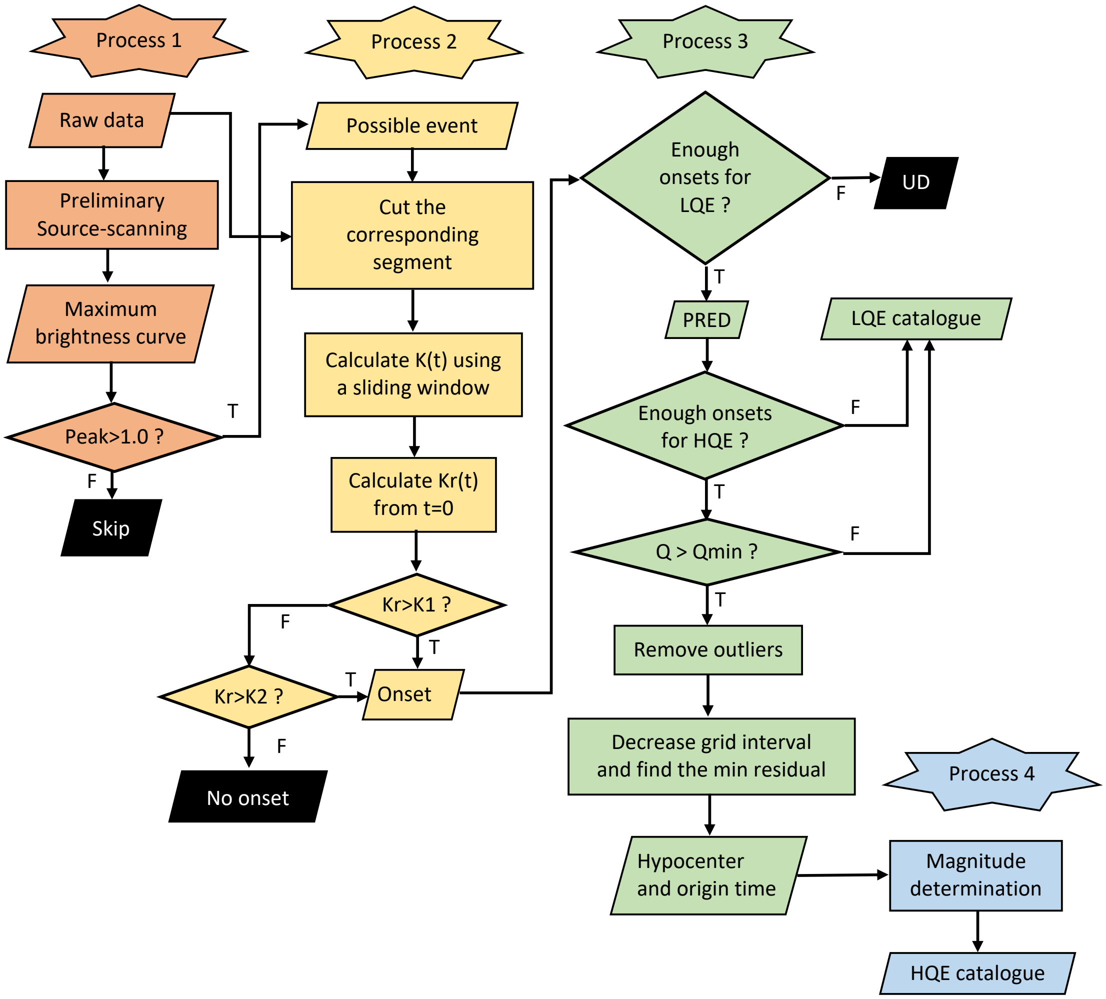

Figure 3.1: The flow chart for S-SNAP. Process 1 is preliminary source scanning, Process 2 is kurtosis-based phase-picking, Process 3 is locating the source via intersection of EDT layers and travel time residuals, and Process 4 is magnitude determination. HQE, LQE and UD stand for high-quality event, low-quality event and unclear detection, respectively. K and Kr are kurtosis and kurtosis rate. K1 and K2 are two thresholds for phase-picking. PRED is the preliminary solution determined by maximum intersection of EDT layers. Q is event quality, defined as the percentage of layers intersect at the PRED, while Qmin is the quality threshold for high-quality event.

the averaged moment magnitude (M_w) is determined from the distance-corrected Fourier spectra of seismic waveforms recorded at individual stations (Boore, 2003; Atkinson et al., 2008).

3.2.1 Preliminary Source Scanning

The basic idea of source scanning is to assume every grid node in a study area to be a potential source at any time. With a velocity model, the travel time from grid node i to station j can be calculated as tt_{ij}. Assuming that the origin time is t, then for a potential source i, its signal is expected to arrive at station j around the predicted arrival time $t + tt_{ij}$. By stacking all of the N stations' seismogram segments around $t + tt_{ij}$ and calculating the average energy of the stacked trace, the brightness as a function of grid node i and time t is defined as

$$br(i,t) = \frac{1}{N}\sqrt{\frac{1}{win}\sum_{k=1}^{win} S_{it}^2(k)} \tag{3.1}$$

and

$$S_{it}(k) = \sum_{j=1}^{N} |s_j(t + tt_{ij} + (k - \frac{1}{4}win) \times \triangle t)| \tag{3.2}$$

where $k \in (1, win)$, and win is the number of sample points in a waveform segment, $\triangle t$ is the sampling time interval and S is the stacked amplitude from individual seismograms s after alignment with the assumed source location and time. If the assumed location and time correspond to a true seismic source, the brightness value is expected to reach a peak in both time and space domains. Otherwise, it only gives a value indicating the noise.

This direct linear stacking suffers from several problems. First, because the brightness function depends on the amplitude of seismic signals, large amplitudes from non-source effects can significantly contaminate the scanning result. For example, different SNR and absolute amplitude at different stations tend to skew individual stations' brightness contribution that in turn bias the brightness value. Second, segments with extremely large amplitudes may overwhelm the brightness calculation regardless of whether the assumed location and time is correct or not, thus giving rise to artefacts. Finally, the background noise level often varies with time and is inevitably included in the brightness calculation, which means that the brightness threshold for identifying a seismic source may also vary with time.

We introduce two data processing schemes to overcome these problems. We first subdivide the continuous seismogram into 1-min segments and use the median amplitude as the representative noise level of that station within that minute. The individual minute-long segments are then normalized against these median amplitudes such that the normalized noise level of any station is always ~1. Second, we take the third root of the seismograms to suppress anomalously large amplitudes that are clearly unrelated to source signals. As a result, the brightness function is redefined as

$$br(i,t) = \left[\frac{1}{N} \sqrt{\frac{1}{win} \sum_{k=1}^{win} S_{it}^{2}(k)} \right]^{3} \tag{3.3}$$

$$S_{it}(k) = \sum_{j=1}^{N} \left[\frac{|s_j(t + tt_{ij} + (k - \frac{1}{4}win) \times \triangle t)|}{median} \right]^{\frac{1}{3}} \tag{3.4}$$

This revised approach ensures that every station has nearly equal weighting in the stacking process, yet stations with higher SNR can contribute more to the brightness function. Meanwhile, it can successfully reduce the influence of anomalously large non-source amplitudes on brightness calculation. Another benefit is that the roughly constant noise level requires only a single brightness threshold to identify the existence of seismic sources regardless of time.

Following Liao et al. (2012), we process waveform components including P and S phases independently and the final brightness function is given by

$$br = br_P \times br_S \tag{3.5}$$

where br_P and br_S are brightness functions calculated based on P and S travel time tables, respectively.

In each time step, a 3-D brightness distribution is determined (e.g., Fig. 3.3) and the maximum value is found. Those maximum values form a curve as a function of time (e.g., Fig. 3.4). The peaks on that curve above a preset threshold indicate potential events. Based on each potential event's time and location, the waveform segments at individual stations that contain P or S onset are extracted and used in the next stage to navigate the phase-picking process (Fig. 3.1-Process 1).

Although we have taken actions to suppress artefacts, false detections are inevitable when a low brightness threshold (e.g., 1.0, which actually represents the noise level) is used to identify as many potential events as possible. As the trade-off between brightness threshold and false alarm rate is a fundamental issue of SSA, a better strategy is to include as many potential events as possible in the preliminary scanning stage. We depend on the following two processes to address the problem of false detections.

3.2.2 Kurtosis-based Phase-picking

On seismograms, both P and S phases may be recorded in all components. Rather than distinguish P and S onsets and dealing with cross-contamination, we adopt Process 1's preliminary scanning results to ensure that there is only one onset within each time segment cut out from the continuous seismogram, which is already known to be either the P or S arrival of a particular earthquake. Therefore, the task here is much easier than the general problem of seismic phase detection. The characteristic function of kurtosis is chosen to deal with this simple situation. Kurtosis is defined as the fourth standardized moment of a group of sample points X:

$$K = \frac{E[(X-\mu)^4]}{E[(X-\mu)^2]^2} \tag{3.6}$$

where μ is the mean value of X and E denotes the expectation. The kurtosis of a normally distributed dataset is 3. Therefore, a window of seismogram including only Gaussian noise results in $K \approx 3$. On the other hand, the first m points of a seismic onset would break the normal distribution of a sample consisting of M individuals, giving the maximum kurtosis, while including a longer part of a signal lowers K. Therefore, onset time is assigned when a sudden rise occurs in kurtosis value (Fig. 3.1-Process 2). For convenience, we subtract 3 from the kurtosis values so that the noise gives $\sim$0.

We apply a short sliding window (e.g., 1 s) but containing enough sample points (e.g., 500) and move it one sample point each time on the segment to get the kurtosis value of that segment as a function of time, namely, $K(t)$. Then, the kurtosis rate is defined as

$$Kr(t) = K(t + dt) - K(t) \tag{3.7}$$

We first look for an obvious sudden rise from the beginning of the segment. If there is a time step t_0 where $Kr(t)$ reaches a preset threshold K_1, the process stops, and we assign t_0 to be the onset time. If no such time step occurs throughout the entire segment, we then look for the maximum value of $Kr(t)$ and check if it is larger than another preset threshold K_2. If so, the end time of that step minus the time duration of m sample points is assigned to be the onset time. If the two strategies both failed, then no pick is determined, meaning that the entire segment is considered random noise. We note that dt, K_1, K_2 and m are related to data quality, window duration and sampling rate. Usually for a given dataset, their values are fixed.

At the end of this process, we use the total number of picks to classify each event's overall quality into three groups: high quality events (HQE), low quality events (LQE) and uncertain detections (UD) (Fig. 3.1-Process 2).

In most cases, picks are reliable, but occasionally false picks are obtained. The reason could be an unexpected disturbance before the onset, or that two onsets are so close to each other (e.g., $\leq$0.5 s) that they are included in one seismogram segment. This problem is addressed in the next process.

3.2.3 Locating the Source via EDT Layers and Travel Time Residuals

In this process, we adopt the MAXI method and determine the hypocenter of a seismic source in 3 steps. First, we use the arrival times of P and S phases obtained in the previous process to construct the EDT surfaces. Then we set a tolerance level of time error $Terr$ which would expand the EDT surface on both sides into an EDT layer. The grid node with the largest number of intersecting of EDT layers is assigned to be the preliminary hypocenter solution (PRED). For each event with n_P P picks and n_S S picks, the maximum number of intersection of EDT layers at a grid node is

$$MAXI_{ceil} = \frac{n_P \times (n_P - 1)}{2} + \frac{n_S \times (n_S - 1)}{2} \tag{3.8}$$

The quality value is defined as the actual EDT volume number a divided by $MAXI_{ceil}$:

$$Q = \frac{a}{MAXI_{ceil}} \tag{3.9}$$

If Q is smaller than a preset threshold $Qmin$, the event is deemed a LQE despite enough picks being obtained in the previous process. For a LQE, the PRED is considered the final solution.

For HQEs, a final step is performed with progressively finer grids to search iteratively for the minimum average residual between observed and theoretical arrival times. The final solution is declared when the finest grid (at the spacing interval of s) is reached or the decrease of the average residual dr is negligible (i.e., below $p\%$).

One of the biggest advantages of using EDT layers for source location is that phase picks with anomalously large time residuals, either due to false picking or other unknown reasons, form outliers that will have no influence (in relation to the majority of well-behaved picks) in the determination of the PRED. As they will not be used in the final solution, erroneous phase picks cannot contaminate the precision and accuracy of the event's location.

3.2.4 Magnitude Determination

Detailed explanations of using the Fourier spectra to obtain the moment magnitude of an earthquake are available in Boore (2003) and Atkinson et al. (2008). Here, we only provide the formulas for the purpose of reference and completeness. The seismic moment is derived by

$$M_0 = \frac{FD}{C} \tag{3.10}$$

where FD is the median value of Fourier displacements at all stations corrected to r_0=1 km, and

$$C = \frac{RvF}{4\pi \rho r_0 \beta^3} \times 10^{-20} \tag{3.11}$$

where ρ is the density of the source material in g/cm^3, β is the shear wave velocity in km/s, $R = 0.55$, $v = 0.71$, and $F = 2$. The moment magnitude is calculated from the correspond moment as (Hanks & Kanamori, 1979):

$$M_w = \frac{2}{3} \log_{10} M_0 - 10.71 \tag{3.12}$$

where M_0 is expressed in dyne·cm. This process is also totally automatic.

3.3 Application to Induced Seismicity Data

We apply S-SNAP to data from the Tony Creek Dual Microseismic Experiment (ToC2ME), a passive seismic monitoring program that recorded induced seismicity from a 4-well hydraulic-fracturing operation in Alberta, Canada (D. W. Eaton et al., 2018). Sixty eight three-component geophones were installed in shallow wellbores and an accelerometer was installed near the surface (Fig. 3.2), all with a sampling rate of 500 Hz. A detailed velocity model for both P and S waves is available for the area based on well logs to a depth of 3.5 km and derived from crustal refraction profiles below that (Zelt & Ellis, 1989). For the purpose of demonstration, we select three hours of continuous waveform data with distinctive features in this application to illustrate the merits of our method. In the busiest hour (H1, Hour 20 Nov. 5^{th}), 40 events were identified in the ToC2ME catalogue (D. W. Eaton et al., 2018). In the second hour (H2, Hour 14 of Nov. 27^{th}), there were two large earthquakes ($M_w > 1$) and three smaller ones identified. In contrast, the third hour (H3, Hour 8 of Nov. 1^{st}) provides no event in the ToC2ME catalogue. Results of H1 will be discussed first, followed by the other two.

We set the preliminary scanning volume to be a cuboid below the seismic array with a grid interval of $\sim$250 m. We pre-calculate the P and S waves travel times for each grid node-station pair using the software "TauP" (Crotwell et al., 1999).

In the first preliminary scanning process, we use a 1-s time window with a 0.5 s increment to scan through all possible location and time combinations. Given the station distribution, P waves mainly excite the vertical component while S waves

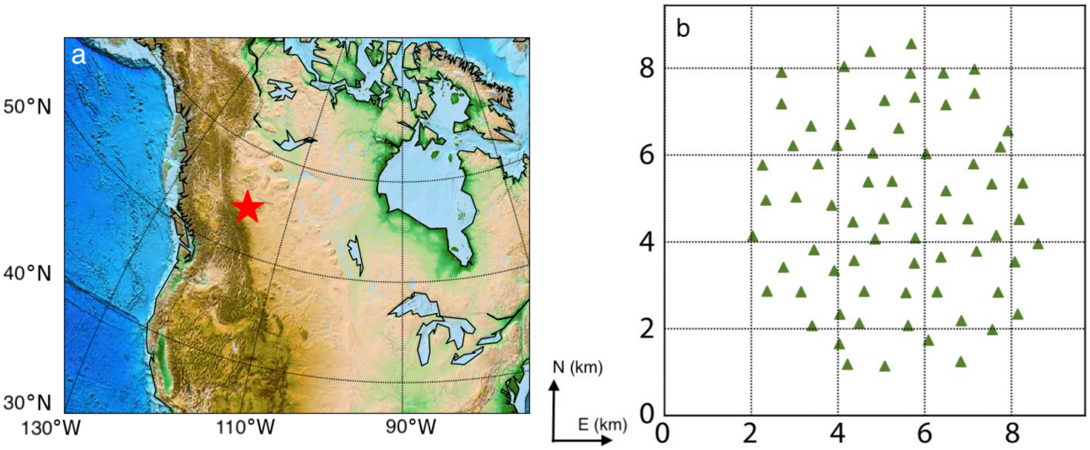

Figure 3.2: (a): Location of ToC2ME program. The red star shows the location of the array in western Canada. (b): Detailed station distribution (green triangles) of ToC2ME program.

mainly excite horizontal components. Thus, we apply the P and S travel time tables to the vertical and horizontal components, respectively. In each time step, we determine 3-D brightness distributions for P and S waves separately and the combined results are used to identify the grid node with the maximum brightness (Eq. 3.5, Fig. 3.3). After the entire hour scanning is finished, we plot each maximum brightness value as a function of time (Fig. 3.4) and take all peaks with brightness value >1.0 (488 in total) as potential events entering the next process. Some of these events are located close to injection wells, as the example shown in Fig. 3.3, but many others are scattered across the study area. Possible reasons for mislocation in this process include the misalignment of seismogram segments, low SNR of the waveform data, and false detections due to contamination of large random noise, as the examples shown in Fig. 3.5.

The second process, kurtosis-based phase-picking, is highly effective in eliminating

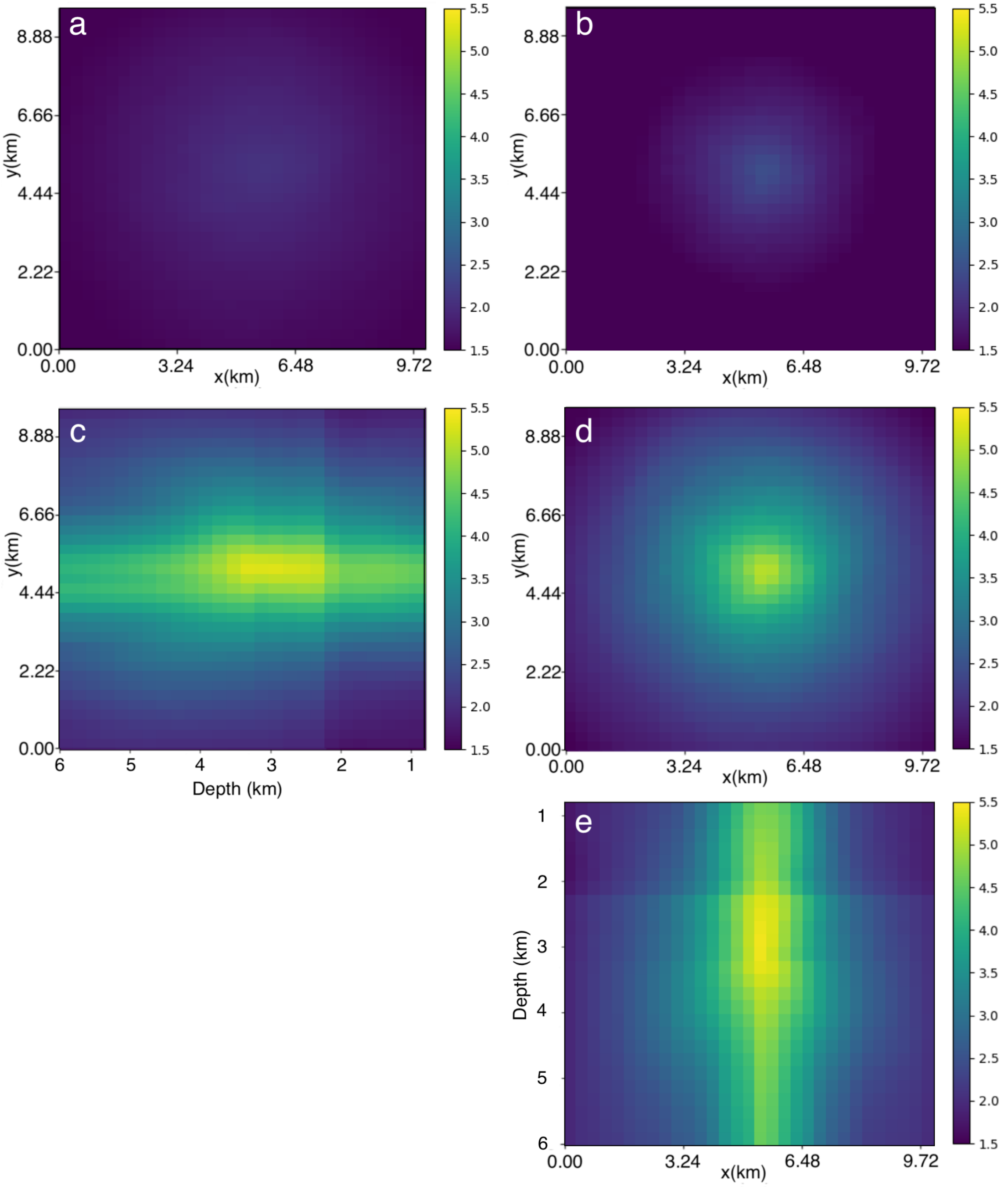

Figure 3.3: Slices including the maximum value of 3-D brightness map in the 36^{th} step (18 s) in H1. (a): Top view of P brightness map. (b): Top view of S brightness map. (c, d, e): Left view, top view and front view of combined brightness map.

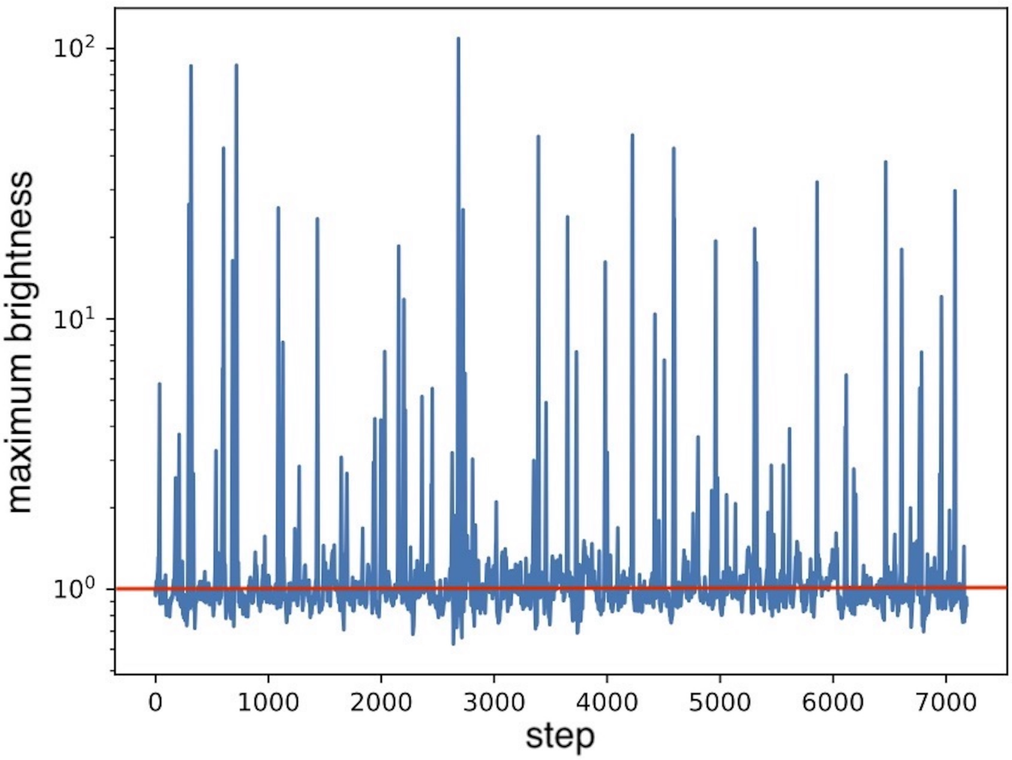

Figure 3.4: Maximum brightness curve for H1. One step is 0.5 s. All peaks above 1.0 (red line) are considered potential events, entering Process 2.

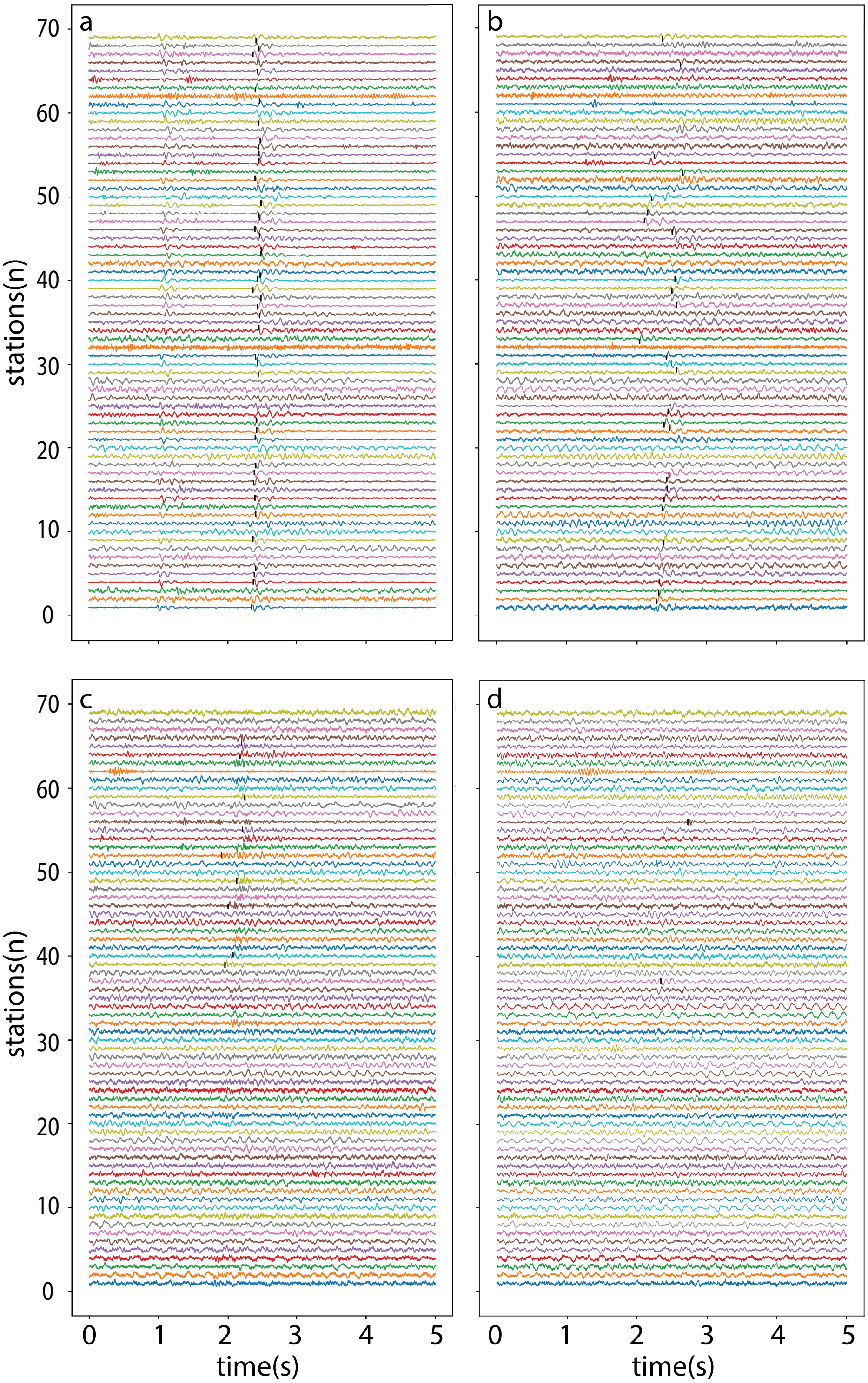

Figure 3.5: Phase-picking examples. (a): S_2 picks of a well aligned HQE (H1, step 179). The event about 1.4 before is also identified as a well aligned HQE. (b): S_1 picks of a poorly aligned HQE (H1, step 216). (c): P picks of a LQE (H1, step 89). (d): P picks of an UD (H1, step 13).

false detections. For this particular application, we use $dt = 5$, $K_1 = 3$, $K_2 = 1$, and $m = 10$ in the kurtosis rate calculation and the identification of a phase onset. We use the average onset time determined from the two horizontal components to be the S arrival. In case that onset time can be determined from only one horizontal component, it is taken as the corresponding S arrival time. We define a HQE event as having at least 15 P and 15 S arrivals. Similarly, a LQE event has 4–14 P or 4–14 S arrivals. Otherwise, the event is classified into the UD category (Fig. 3.5). In total, we have found 125 HQEs, 143 LQEs and 220 UDs (Table 3.1).

In the next process of locating HQEs and LQEs with the MAXI method, we set $Terr = 0.1\ s$ to accommodate possible difference between the theoretical and observed arrival times due to the imperfect velocity model. We also demand the quality value Q (Eq. 3.9) to be at least 0.5 for HQEs. Two events are downgraded from HQE to LQE as a result of this additional requirement (Table 3.1). In searching the final solutions, we set the smallest grid interval (s) and the residual improvement percentage (p) to be 1 m and 0.1, respectively. For most HQE events, the minimum residual can be obtained with a spatial resolution between 1 and 10 m. The average and median values of travel time residual for all 123 HQEs are both 0.04 s. The 3-D distribution of HQE hypocenters is shown in Fig. 3.6. They concentrate in a small area surrounding the injection wells with a linear NE-SW-trending pattern. Their depths fall in a narrow range around 3250 m, which is ∼200 m above the hydraulic fracturing depth of about 3445 m. A sharp alignment of the events occurs at 3267 m where there is a big discontinuity in the velocity model. We tend to interpret this as an artefact caused by the inaccurate layered model. However, it is also possible

Table 3.1: Summarized results for all three hours.

Hour	HQE(P2/F)	LQE(P2/F)	UD	Total	M_w Range (HQE)
H1	125/123	143/145	220	488	-0.21 to 0.33
H2	19/19	74/74	494	587	-0.15 to 1.72
H3	17/17	111/111	470	598	-0.14 to 0.01

Note. "P2" means results in "Process 2" while "F" means final results. HQE, LQE and UD stand for high-quality event, low-quality event and unclear detection.

that the earthquakes stop at that depth due to different physical properties, such as rheology, permeability, and stress state.

The 3-D distribution of HQE hypocenters for H2 and H3 are also presented in Fig. 3.6. The focal depths of all these events are remarkably consistent with the results for H1. The hypocenters are all located near the wells but with linear patterns different from the one identified for H1, probably corresponding to different fault systems. The numbers of events of different solution qualities are summarized in Table 3.1 for all three selected hours.

For M_w determination, we get ρ and β from the velocity model according to the event depth. The results are also summarized in Table 3.1.

In general, the performance of S-SNAP is stable and consistent regardless of the number of events in each hour or the magnitude range. Taking H1 for example, we obtained 268 solutions (123 HQEs and 145 LQEs), equivalent to one event every 13 s on average. For H2 and H3, the average occurrence rate is one event per 39 and 28 s, respectively. Magnitudes in H1 range between -0.21 and 0.33. There are two relatively large events in H2 with M_w of 1.72 and 1.01. In H3, there is no event larger than $M_w = 0.01$. We have verified all HQEs by visually examining their waveform segments and no false detections occurred.

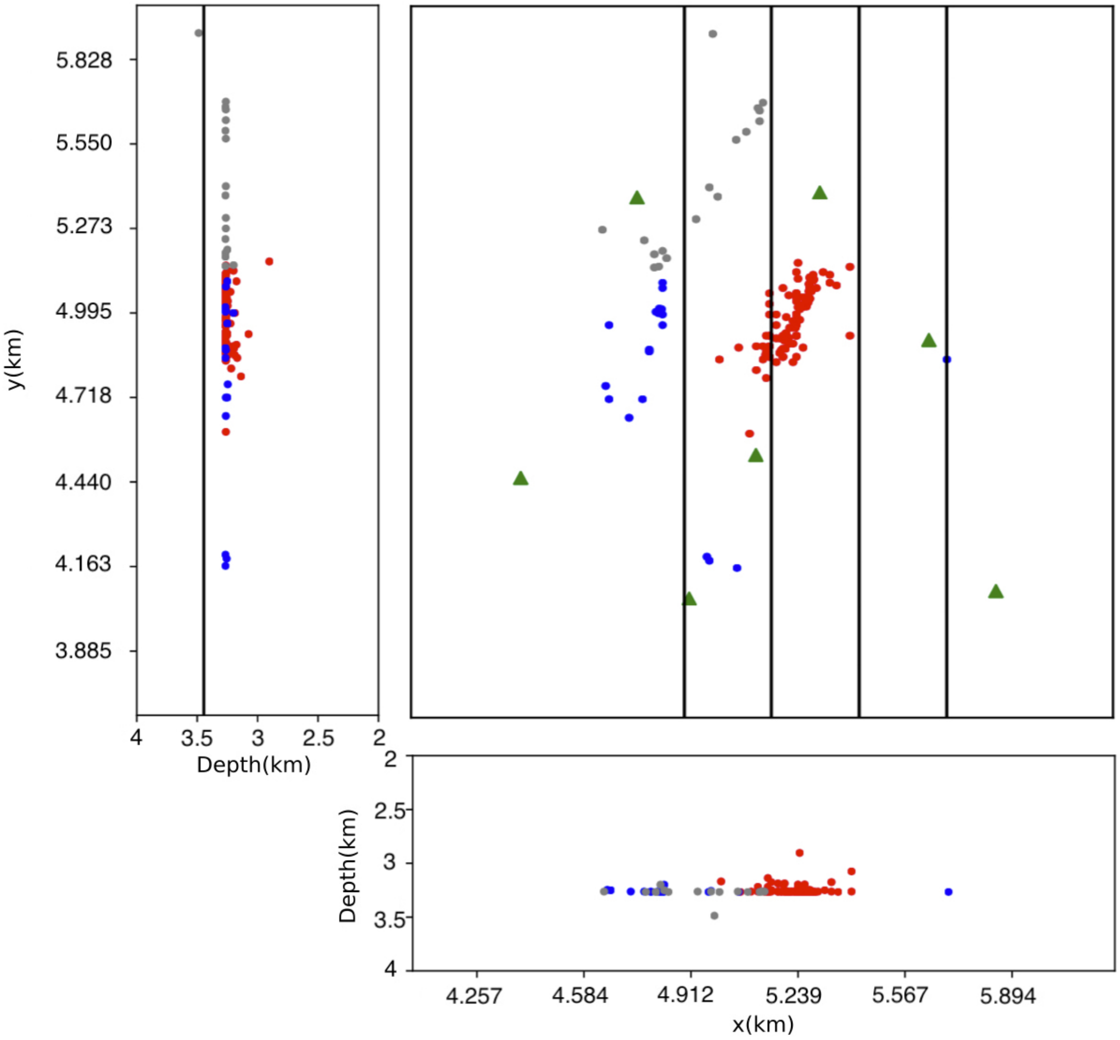

Figure 3.6: HQE locations for H1(red), H2(blue), and H3(grey). Black lines show the locations and depth of the horizontal wells.

Table 3.2: Comparison between S-SNAP and ToC2ME catalogues for all three hours.

Hour	Absolute time	Class	S-SNAP	ToC2ME
H1	Nov. 5th hr 20	HQE	123	40
		LQE	145	108
		UD	220	44
		Total	488	192
H2	Nov. 27th hr 14	HQE	19	5
		LQE	74	23
		UD	494	24
		Total	587	52
H3	Nov. 1st hr 8	HQE	17	0
		LQE	111	19
		UD	470	26
		Total	598	45

3.4 Discussion

The advantage of S-SNAP can be summarized in two aspects: 1) the process is completely automatic and highly efficient, and 2) the result is accurate, consistent and comprehensive. Because no human intervention is required during the entire process, the S-SNAP result does not suffer from any interpreter bias. The processing time depends largely on the number of events in the dataset. Using a modest computer cluster with 22 nodes, it takes ∼80 min to process the busiest hour (H1, Table 3.1) with 123 HQEs out of more than 480 detections. By increasing the parallel computing capacity of the cluster, it is theoretically possible to run S-SNAP in near-real-time mode for automatic earthquake monitoring and precise location.

We compare our results with the seismicity catalogue obtained by the original ToC2ME study (D. W. Eaton et al., 2018) to further illustrate the advantages of S-SNAP (Table 3.2). The ToC2ME catalogue was obtained using a template-matching method and verified by visual inspection, thus is considered free from artifact events.

It is very encouraging that all HQEs in the ToC2ME catalogue are included in the S-SNAP catalogue with similar original times and epicenters. The M_w values between the two catalogues are very consistent for events with $M_w = 0.2$ or larger, while smaller events appear to show more scatter. In terms of focal depth, the S-SNAP results are more consistent and concentrated (Fig. 3.6).

Overall, S-SNAP found nearly four times as many HQEs (159 events vs. 45 events, Table 3.2). Taking the numbers of HQE and LQE together, our catalogue has about 2.5 times as many events as the ToC2ME catalogue (489 events vs. 195 events, Table 3.2). Given the almost identical definition of HQE (at least 15 stations recording both P and S arrivals are required in the ToC2ME catalogue while our threshold is 15 P-phase and 15 S-phase picks), these numbers demonstrate that S-SNAP can be a powerful tool for delineating the detailed spatiotemporal distribution of induced seismicity in the vicinity of injection sites. In addition, this disparity of event numbers may be caused by template bias in ToC2ME catalogue, which in turn reflects one of the advantages of S-SNAP that every event is independent, so that it can provide a more comprehensive catalogue.

We acknowledge that seismic station coverage as dense as the ToC2ME array is extraordinary and usually unavailable for most seismic experiments. To test the performance of S-SNAP with a sparser array, we repeat the location process using H1 data with decreasing numbers of stations (Table 3.3). As expected, the number of HQE solutions decreases with fewer stations. However, even with only 7 stations (about one tenth of the available stations), S-SNAP still identifies 61 HQEs, which is ~50% more of that in the ToC2ME catalogue. A few events are identified as new

Table 3.3: Comparison among different station numbers using H1 data.

Number of stations	HQE numbers	Threshold	Max diff (m)	Mean diff (m)
69	123	15		
69	134	10		
35	113	10	209	50
23	93	10	391	57
14	80	7	412	101
7	61	5	567	124
69 (ToC2ME)	40	15		

Note. Threshold means the minimum number of P and S arrivals picked to be a HQE.

HQEs because of the lower thresholds, and all of them are located within or near the event cluster.

We define the hypocentral difference as the distance between the hypocenter determined by all 69 stations (S-SNAP catalogue) and that by fewer stations. If a new event is detected, the original location is simply assumed to be at the center of the cluster. Our experiment results show that all HQE solutions are stable (hypocentral difference <600 m) and no false detections were produced by eliminating stations. Both the maximum and average hypocentral differences increase with fewer stations; however, the mean value is always much smaller than 250 m.

Figure 3.7 shows the extreme example of using only 7 stations. When compared to the results with all 69 stations, the linear pattern of epicenters remains unchanged and most solutions stay at the same depth (∼3250 m). The majority of the events have hypocentral difference less than 150 m (Fig. 3.8). The result of this experiment demonstrates that, even with only one tenth of the total stations, S-SNAP can still perform reliably and produce a catalogue more comprehensive than the original ToC2ME catalogue with no false detections. More significantly, the required calculation time decreases dramatically by $\sim$ 86% from $\sim$80 min with 22 nodes to only $\sim$30 min with 8 nodes.

Ideally, the threshold for HQE should be set in such a way that the maximum number of events can be located with tolerable uncertainty and no false detections. When there are more than 30 stations, the result is not very sensitive to the threshold because the number of phase arrivals are often more than what is required to derive a stable solution for most events. As shown in Table 3.3, using 10 and 15 as the thresholds for 69 stations only makes less than 10% change in the number of HQE. However, with fewer than 20 stations, the threshold should be half of the total number of stations to ensure the solution quality. We find that a threshold of 5 stations is the lower limit for all cases. The empirical relationship between the choice of threshold for HQE and the total number of available stations is presented in Fig. 3.9.

Similarly, we test the performance of S-SNAP with different scenarios of azimuthal gap. Fig. 3.6 shows the result with the total 69 stations (at least one station every 15°). In a series of experiments, we use the H1 data and repeat the location process with stations located only on the northern side (azimuthal gap=180°, Fig. 3.10a), in the northwestern quadrant (azimuthal gap=270°, Fig. 3.10b), and in the NWW wedge area (azimuthal gap=315°, Fig. 3.10c). When compared the results of 180° and 270° azimuthal gap to the original catalogue, the average hypocentral difference is on the order of 100 m with the maximum less than 500 m. However, if the gap is as large as 315°, the worst event is mislocated by as much as 4 km and the mean difference increases to about 500 m, almost twice of the original uncertainty. Thus, the upper limit of azimuthal gap for S-SNAP in this case is about 270°.

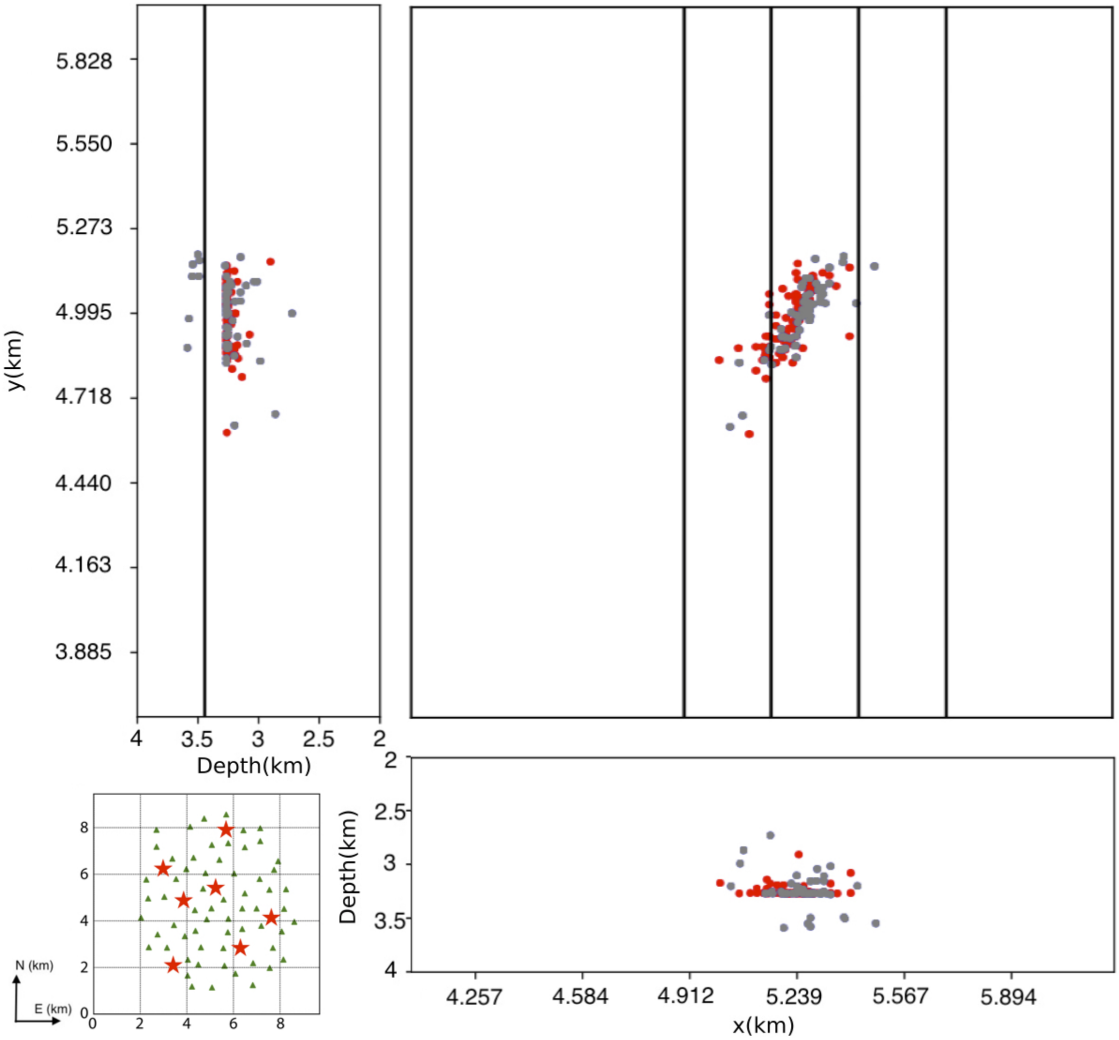

Figure 3.7: HQE locations by 7 stations with at least 5 *P* and 5 *S* picks (grey) and 69 stations with at least 15 *P* and 15 *S* picks (red) for H1. Black lines show the locations and depth of the horizontal wells. Inset shows the 7 selected stations (red stars) out of 69 (green triangles).

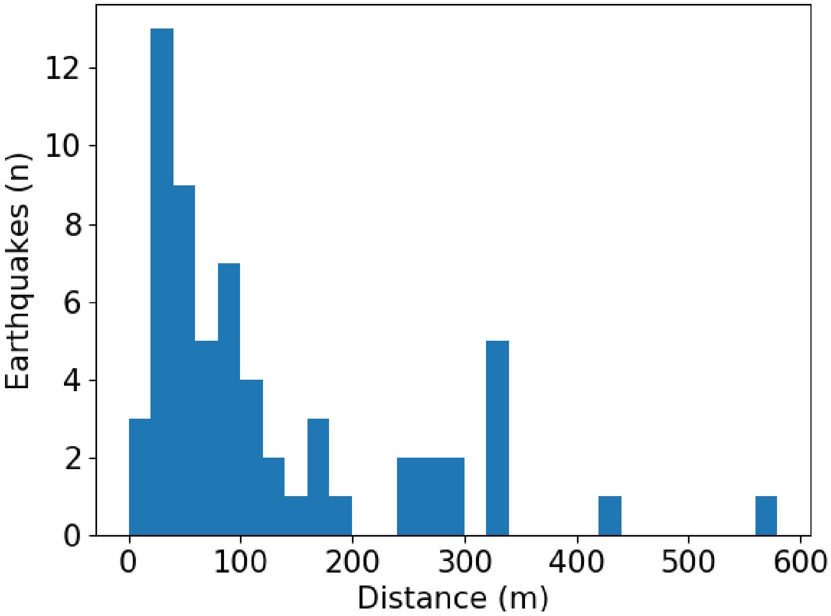

Figure 3.8: Histogram of hypocentral difference between locations derived by 7 stations and 69 stations.

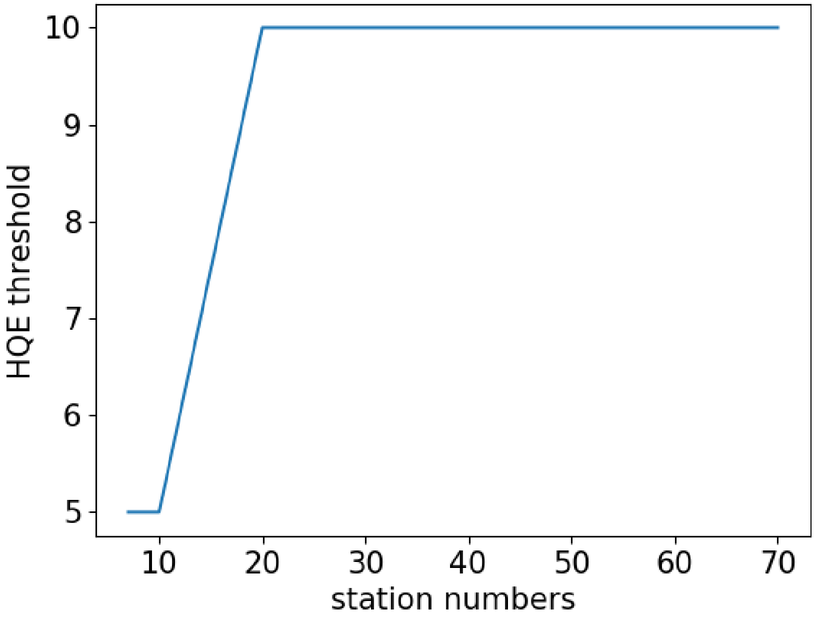

Figure 3.9: Recommended HQE threshold for different station numbers.

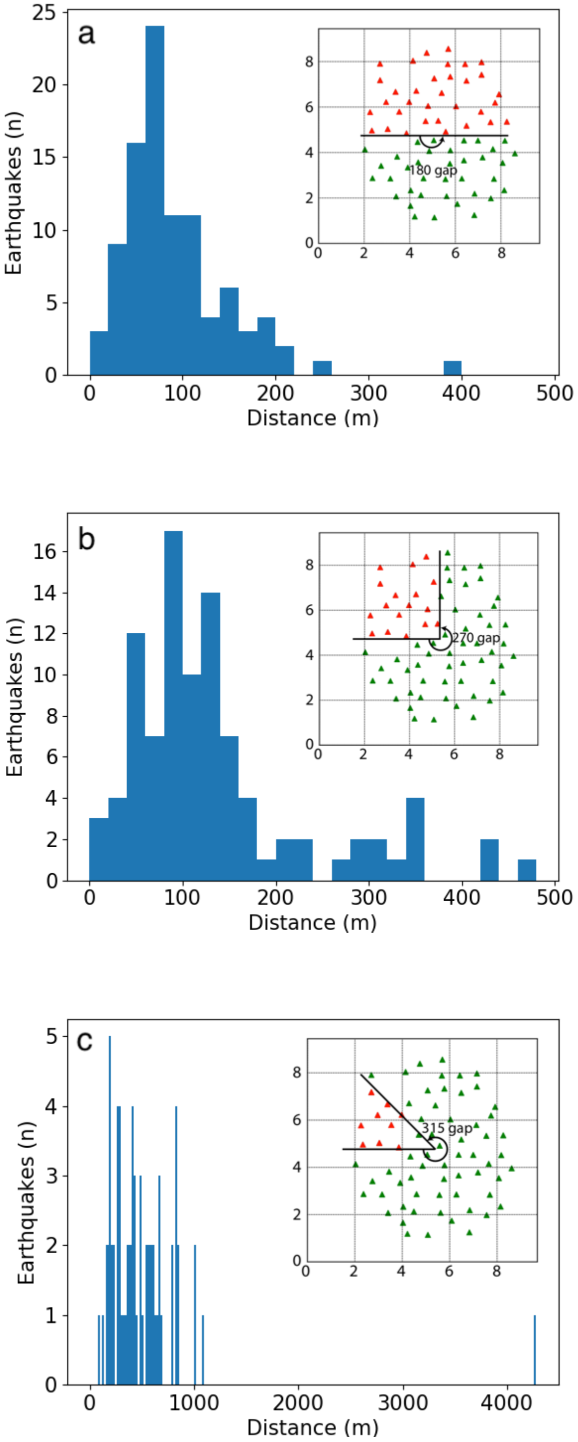

Figure 3.10: Station distributions for different azimuthal gaps and corresponding histograms of hypocentral difference compared with results from 69 stations. Green triangles represent all the stations while red color highlights the used ones in each test. The width of each rectangle is 20 m.

We note that the brightness threshold used in the preliminary scanning (i.e., Process 1) is important. In theory, the preliminary scanning results are more reliable when a higher threshold is used. The trade-off, however, is the high possibility of missing events. On the other hand, if a lower threshold is used in Process 1, the results are more comprehensive but with many artifacts. In this study, we take the most conservative approach by setting it at 1.0, which is equivalent to the mean value of random noise. The main rationale for using this approach is that S-SNAP relies on the preliminary scanning (i.e., Process 1) to ensure the completeness of the catalogue. Because the issue of eliminating artefacts can be properly handled by subsequent processes, we recommend that this threshold should be set as low as reasonably possible. A higher brightness threshold can jeopardize the completeness of S-SNAP results.

Scanning increment and window duration also play important roles. The time window should be long enough to include the whole P or S wave train (in this case, less than one second for $M_w \leq 2$ earthquakes), whereas the increment should be smaller than the window duration. Shorter increment and duration lead to higher time resolution, but they may fail to correctly identify larger earthquakes with longer source time functions. The scanning parameters used in this study (1 s window and 0.5 s increment) are able to resolve two events that are only $\sim$1.4 s apart in origin time. However, we note that such high time resolution may only be possible if the two events are comparable in size. In case that one of the events is much larger than the other, the brightness peak of the smaller one may be buried in the peak of the larger one, making it invisible to preliminary scanning.

We have conducted a number of experiments by taking the second, third or fourth root of the input data before stacking. The results show that the second root is insufficient to diminish the dominance of spurious signals from some stations while the fourth root sometimes suppresses true signals too harshly. However, different conclusions may be reached for different data sets (e.g., Muirhead & Datt, 1976; Xu et al., 2009). We also tried setting an upper limit for the data points so that any value exceeding that “cap” is suppressed. However, this approach reduces the time resolution and the issue of selecting the optimal “cap” value is difficult to determine *a priori*.

In the phase-picking process, we calculate $Kr(t)$ with $dt = 5$ sample points. This value comes from the result of a series of experiments with dt ranging from 1 to 10. Our experiments show that $dt = 4$, 5 or 6 all give similarly good results. Based on this, we found that $Kr(t)$ reaches a maximum 5 to 20 sample points after the onset in most cases. This is the main reason that we take $m = 10$ in our application. We suggest that dt and m can be fixed in applying S-SNAP to different datasets. The $Kr(t)$ threshold K_2 depends on the signal-to-noise ratio of the dataset. While $K_1 = 3$ can pick out good signals, K_2 includes more possible onsets. In the high quality ToC2ME dataset, $K_2 = 1$ hardly adds any false positives. However, this value should be raised to 1.5 or 2 in noisier cases.

Chapter 4 Conclusion and Future Works

Beamforming is a useful tool in many types of seismological analysis, especially when incorporated with other techniques to deal with more complex situations. We provide improved methodologies, 3-D PWBP and S-SNAP in this thesis.

The 3-D PWBP method shows higher spatial resolution than standard BP and many variants; however, it is still not enough to fully distinguish all the faults in a large and complex rupture scenario such as the 2016 Kaikōura earthquake. We envisage that it can be further improved in the future by incorporating teleseismic waveforms from multiple arrays along different azimuthal ranges to maximize data resolution and mitigate artefacts. This is made possible with the increasing number of dense regional and local broadband seismograph arrays around the world in recent years. Nevertheless, we acknowledge that in practice, using teleseismic data alone may be difficult to image the spatiotemporal rupture of a major earthquake in great detail. Developing a suitable framework for 3-D PWBP to incorporate other datasets, such as seismic waveforms at regional and/or local distances as well as high-rate GPS/GNSS time series, may provide further improvements. Also, with the 3-D PWBP results, we could gain more insight about rupture physics in the future.

The S-SNAP method successfully fulfills the objective of automatic earthquake detection and location with high completeness and accuracy. The performance can also be efficient when it is implemented in a parallel-computing environment. Application to real seismic data collected during hydraulic fracturing operations has demonstrated S-SNAP's advantages in detecting and locating induced earthquakes that are clustered in both time and space. We plan to expand the application of S-SNAP to other difficult problems that most conventional methods may fail, such as the determination of hypocenters of the extremely high number of aftershocks during the first few hours or days of a major earthquake or the detection of very small earthquakes in a noisy environment. The more comprehensive earthquake catalogues produced by S-SNAP can also provide much more insight for seismotectonic studies. Furthermore, they can be used as a much better training set in many machine-learning applications to enhance the accuracy of model prediction as well.

Bibliography

Akram, J., & Eaton, D. W. (2016, March). A review and appraisal of arrival-time picking methods for downhole microseismic data. *Geophysics*, *81*(2), KS71–KS91. doi: 10.1190/geo2014-0500.1

Allen, R. (1978, October). Automatic earthquake recognition and timing from single traces. *Bulletin of the Seismological Society of America*, *68*(5), 1521–1532.

Allen, R. (1982, December). Automatic phase pickers: their present use and future prospects. *Bulletin of the Seismological Society of America*, *72*(6B), S225–S242.

Atkinson, G. M., Kaka, S. I., Eaton, D., Bent, A., Peci, V., & Halchuk, S. (2008, January). A very close look at a moderate earthquake near Sudbury, Ontario. *Seismological Research Letters*, *79*(1), 119–131. doi: 10.1785/gssrl.79.1.119

Baer, M., & Kradolfer, U. (1987, August). An automatic phase picker for local and teleseismic events. *Bulletin of the Seismological Society of America*, *77*(4), 1437–1445.

Bai, L., Wu, Z., Zhang, T., & Kawasaki, I. (2006, February). The effect of distribution of stations upon location error: statistical tests based on the double-difference earthquake location algorithm and the bootstrap method. *Earth, Planets and Space*, *58*(2), e9–e12. doi: 10.1186/BF03353364

Bai, Y., Lay, T., Cheung, K. F., & Ye, L. (2017). Two regions of seafloor deformation generated the tsunami for the 13 November 2016, Kaikoura, New Zealand earthquake. *Geophysical Research Letters*, *44*(13), 6597–6606. (2017GL073717) doi: 10.1002/2017GL073717

Baillard, C., Crawford, W. C., Ballu, V., Hibert, C., & Mangeney, A. (2014, February). An automatic kurtosis-based P- and S-phase picker designed for local seismic networks. *The Bulletin of the Seismological Society of America*, *104*, 394–409. doi: 10.1785/0120120347

Barry, H. J. (1968, February). *Beam forming system* (No. US3370267A).

Berberian, M., Jackson, J. A., Qorashi, M., Khatib, M. M., Priestley, K., Talebian, M., & Ghafuri-Ashtiani, M. (1999). The 1997 May 10 Zirkuh (Qa'enat) earthquake (Mw 7.2): faulting along the Sistan suture zone of eastern Iran. *Geophysical Journal International*, *136*(3), 671–694. doi: 10.1046/j.1365-246x.1999.00762.x

Boore, D. M. (2003, March). Simulation of ground motion using the stochastic method. *Pure and Applied Geophysics*, *160*(3-4), 635–676. doi: 10.1007/PL00012553

Bostock M. G., Royer A. A., Hearn E. H., & Peacock S. M. (2012, November). Low frequency earthquakes below southern Vancouver Island. *Geochemistry, Geophysics, Geosystems*, *13*(11). doi: 10.1029/2012GC004391

Cesca, S., Zhang, Y., Mouslopoulou, V., Wang, R., Saul, J., Savage, M., … Dahm, T. (2017). Complex rupture process of the Mw 7.8, 2016, Kaikoura earthquake, New Zealand, and its aftershock sequence. *Earth and Planetary Science Letters*, *478*, 110 - 120. doi: https://doi.org/10.1016/j.epsl.2017.08.024

Clark, K. J., Nissen, E. K., Howarth, J. D., Hamling, I. J., Mountjoy, J. J., Ries, W. F., … Strong, D. T. (2017). Highly variable coastal deformation in the 2016 M_W7.8 Kaikōura earthquake reflects rupture complexity along a transpressional plate boundary. *Earth and Planetary Science Letters*, *474*, 334-344. doi: 10.1016/j.epsl.2017.06.048

Crotwell, H. P., Owens, T. J., & Ritsema, J. (1999, March). The TauP toolkit: flexible seismic travel-time and ray-path utilities. *Seismological Research Letters*, *70*(2), 154–160. doi: 10.1785/gssrl.70.2.154

Dai, H., & MacBeth, C. (1997, July). The application of back-propagation neural network to automatic picking seismic arrivals from single-component recordings. *Journal of Geophysical Research: Solid Earth*, *102*(B7), 15105–15113. doi: 10.1029/97JB00625

Duputel, Z., & Rivera, L. (2017, April). Long-period analysis of the 2016 Kaikoura earthquake. *Physics of the Earth and Planetary Interiors*, *265*, 62–66. doi: 10.1016/j.pepi.2017.02.004

Dziewoński, A. M., Chou, T.-A., & Woodhouse, J. H. (1981, April). Determination of earthquake source parameters from waveform data for studies of global and regional seismicity. *Journal of Geophysical Research: Solid Earth*, *86*(B4), 2825–2852. doi: 10.1029/JB086iB04p02825

Eaton, D. W. (2018). *Passive seismic monitoring of induced seismicity: fundamental principles and application to energy technologies*. Cambridge University Press.

Eaton, D. W., Igonin, N., Poulin, A., Weir, R., Zhang, H., Pellegrino, S., & Rodriguez, G. (2018). Induced seismicity characterization during hydraulic fracture monitoring with a shallow wellbore geophone array and broadband sensors. *Seismological Research Letters*. doi: 10.1785/0220180055

Eaton, J. P. (1970). *HYPOLAYR, a computer program for determining hypocenters of local earthquakes in an earth consisting of uniform flat layers over a half space* (USGS Numbered Series No. 69-85). U.S. Geological Survey,.

Efron, B. (1979, January). Bootstrap methods: another look at the Jackknife. *Ann. Statist.*, *7*(1), 1–26. doi: 10.1214/aos/1176344552

Ekström, G., Nettles, M., & Dziewoński, A. M. (2012, June). The global CMT project 2004-2010: centroid-moment tensors for 13,017 earthquakes. *Physics of the Earth and Planetary Interiors*, *200-201*, 1–9. doi: 10.1016/j.pepi.2012.04.002

Fan, W., & Shearer, P. M. (2017, October). Investigation of backprojection uncertainties with M6 earthquakes. *Journal of Geophysical Research: Solid Earth*, *122*(10), 7966–7986. doi: 10.1002/2017JB014495

Font, Y., Kao, H., Lallemand, S., Liu, C.-S., & Chiao, L.-Y. (2004, August). Hypocentre determination offshore of eastern Taiwan using the Maximum Intersection method. *Geophys J Int*, *158*(2), 655–675. doi: 10.1111/j.1365-246X.2004.02317.x

Gilbert, F., & Backus, G. (1968). Elastic-gravitational vibrations of a radially stratified sphere. *Dynamics of Stratified Solids*, 82–95.

Hamling, I. J., Hreinsdóttir, S., Clark, K., Elliott, J., Liang, C., Fielding, E., … Stirling, M. (2017). Complex multifault rupture during the 2016 Mw 7.8 Kaikoura earthquake, New Zealand. *Science*. doi: 10.1126/science.aam7194

Hanks, T. C., & Kanamori, H. (1979, May). A moment magnitude scale. *Journal of Geophysical Research B*, *84*(B5), 2348–2350.

Herrmann, R. B. (1979, April). Fasthypo: a hypocenter location program. *Seismological Research Letters*, *50*(2), 25–38. doi: 10.1785/gssrl.50.2.25

Holden, C., Kaneko, Y., D'Anastasio, E., Benites, R., Fry, B., & Hamling, I. J. (2017). The 2016 Kaikoura earthquake revealed by kinematic source inversion and seismic wavefield simulations: slow rupture propagation on a geometrically complex crustal fault network. *Geophysical Research Letters*, *44*(22), 11,320–11,328. (2017GL075301) doi: 10.1002/2017GL075301

Hollingsworth, J., Ye, L., & Avouac, J.-P. (2017). Dynamically triggered slip on a splay fault in the Mw 7.8, 2016 Kaikoura (New Zealand) earthquake. *Geophysical Research Letters*, *44*(8), 3517–3525. (2016GL072228) doi: 10.1002/2016GL072228

Ishii, M. (2011). High-frequency rupture properties of the Mw 9.0 off the pacific coast of Tohoku earthquake. *Earth, Planets and Space*, *63*(7), 18. doi: 10.5047/eps.2011.07.009

Ishii, M., Shearer, P. M., Houston, H., & Vidale, J. E. (2005). Extent, duration and speed of the 2004 Sumatra-Andaman earthquake imaged by the Hi-Net array. *Nature*, *435*(7044), 933–936.

Ishii, M., Shearer, P. M., Houston, H., & Vidale, J. E. (2007). Teleseismic P wave imaging of the 26 December 2004 Sumatra-Andaman and 28 March 2005 Sumatra earthquake ruptures using the Hi-net array. *Journal of Geophysical Research: Solid Earth*, *112*(B11). (B11307) doi: 10.1029/2006JB004700

Jia, Z., Ni, S., Chu, R., & Zhan, Z. (2017, January). Joint inversion for earthquake depths using local waveforms and amplitude spectra of Rayleigh waves. *Pure and Applied Geophysics*, *174*(1), 261–277. doi: 10.1007/s00024-016-1373-1

Kaiser, A., Balfour, N., Fry, B., Holden, C., Litchfield, N., Gerstenberger, M., ... Gledhill, K. (2017). The 2016 Kaikoura, New Zealand, earthquake: preliminary seismological report. *Seismological Research Letters*, *88*(3), 727. doi: 10.1785/0220170018

Kao, H., & Shan, S.-J. (2004, May). The Source-Scanning Algorithm: mapping the distribution of seismic sources in time and space. *Geophysics Journal International*, *157*(2), 589–594. doi: 10.1111/j.1365-246X.2004.02276.x

Küperkoch, L., Meier, T., Lee, J., & Friederich, W. (2010, May). Automated determination of P-phase arrival times at regional and local distances using higher order statistics. *Geophysics Journal International*, *181*(2), 1159–1170. doi: 10.1111/j.1365-246X.2010.04570.x

Lee, W. H., & Lahr, J. C. (1975). *HYPO71 (revised; a computer program for determining hypocenter, magnitude, and first motion pattern of local earthquakes* (USGS Numbered Series No. 75-311). U.S. Dept. of the Interior, Geological Survey, National Center for Earthquake Research,.

Liao, Y., Kao Honn, Rosenberger Andreas, Hsu ShuKun, & Huang BorShouh. (2012, May). Delineating complex spatiotemporal distribution of earthquake aftershocks: an improved Source-Scanning Algorithm. *Geophysical Journal International*, *189*(3), 1753–1770. doi: 10.1111/j.1365-246X.2012.05457.x

Litchfield, N. J., Villamor, P., Dissen, R. J. V., Nicol, A., Barnes, P. M., Barrell, D. J. A., ... Zinke, R. (2018). Surface rupture of multiple crustal faults in the 2016 Mw 7.8 Kaikoura, New Zealand, earthquake. *Bulletin of the Seismological Society of America*. doi: 10.1785/0120170300

Liu, Z., & Ge, Z. (2015). Rupturing process of the Mw 7.9 Nepal earthquake inverted by the multi-array compressive sensing method. *Chinese Journal of Geophysics*, *58*, 1891–1899. doi: 10.6038/cjg20150605

Liu, Z., Song, C., & Ge, Z. (2018). Utilizing Back-Projection method based on 3-D global tomography model to investigate Mw 7.8 New Zealand south island earthquake. *Acta Scientiarum Naturalium Universitatis Pekinensis*, *54*(4), 721–729. doi: 10.13209/j.0479-8023.2017.105

Liu, Z., Song, C., Meng, L., Ge, Z., Huang, Q., & Wu, Q. (2017). Utilizing a 3D global Pwave tomography model to improve backprojection imaging: a case study of the 2015 Nepal earthquake. *Bulletin of the Seismological Society of America*, *107*(5), 2459. doi: 10.1785/0120170091

Lomax, A., Virieux, J., Volant, P., & Berge-Thierry, C. (2000). Probabilistic earthquake location in 3d and layered models. In C. H. Thurber & N. Rabinowitz (Eds.), *Advances in Seismic Event Location* (pp. 101–134). Dordrecht: Springer Netherlands. doi: 10.1007/978-94-015-9536-0_5

Meng, L., Ampuero, J.-P., Luo, Y., Wu, W., & Ni, S. (2012). Mitigating artifacts in back-projection source imaging with implications on frequency- dependent properties of the Tohoku-Oki earthquake. *Earth Planets and Space*, *64*(12).

Meng, L., Ampuero, J.-P., Sladen, A., & Rendon, H. (2012). High-resolution back-projection at regional distance: application to the Haiti M7.0 earthquake and comparisons with finite source studies. *Journal of Geophysical Research: Solid Earth*, *117*(B4). doi: 10.1029/2011JB008702

Meng, L., Inbal, A., & Ampuero, J.-P. (2011, April). A window into the complexity of the dynamic rupture of the 2011 Mw 9 Tohoku-Oki earthquake. *Geophysical Research Letters*, *38*(7). doi: 10.1029/2011GL048118

Morishita, Y., Kobayashi, T., Fujiwara, S., & Yarai, H. (2017). Complex crustal deformation of the 2016 Kaikoura, New Zealand, earthquake revealed by ALOS. *Bulletin of the Seismological Society of America*, *107*(6), 2676–2686. doi: 10.1785/0120170143

Muirhead, K. T., & Datt, R. (1976). The N-th root process applied to seismic array data. *Geophysical Journal of the Royal Astronomical Society*, *47*(1), 197–210. doi: 10.1111/j.1365-246X.1976.tb01269.x

Neidell, N., & Taner, M. (1971, June). Semblance and other coherency measures for multichannel data. *GEOPHYSICS*, *36*(3), 482–497. doi: 10.1190/1.1440186

Nelson, G. D., & Vidale, J. E. (1990, April). Earthquake locations by 3-D finite-difference travel times. *Bulletin of the Seismological Society of America*, *80*(2), 395–410.

Perol, T., Gharbi, M., & Denolle, M. (2018, February). Convolutional neural network for earthquake detection and location. *Science Advances*, *4*(2), e1700578. doi: 10.1126/sciadv.1700578

Ross, Z. E., Meier, M.-A., Hauksson, E., & Heaton, T. H. (2018, October). Generalized seismic phase detection with deep learning. *Bulletin of the Seismological Society of America*, *108*(5A), 2894–2901. (arXiv: 1805.01075) doi: 10.1785/0120180080

Rost, S., & Thomas, C. (2002). Array seismology: methods and applications. *Reviews of Geophysics*, *40*(3), 2–1–2–27. doi: 10.1029/2000RG000100

Rusnak, G. A. (1969, November). *Beamforming in seismic surveying* (No. US3479638A).

Schimmel, M., & Paulssen, H. (1997). Noise reduction and detection of weak, coherent signals through phase-weighted stacks. *Geophysical Journal International*, *130*(2), 497–505. doi: 10.1111/j.1365-246X.1997.tb05664.x

Simmons, N. A., Myers, S. C., Johannesson, G., & Matzel, E. (2012). LLNL-G3Dv3: Global P wave tomography model for improved regional and teleseismic travel time prediction. *Journal of Geophysical Research: Solid Earth*, *117*(B10), n/a–n/a. (B10302) doi: 10.1029/2012JB009525

Sudhaus, H., & Jónsson, S. (2011). Source model for the 1997 Zirkuh earthquake (MW= 7.2) in Iran derived from JERS and ERS InSAR observations. *Geophysical Journal International*, *185*(2), 676–692. doi: 10.1111/j.1365-246X.2011.04973.x

Takeuchi, H., & Saito, M. (1972). Seismic surface waves. In B. A. BOLT (Ed.), *Seismology: Surface waves and earth oscillations* (Vol. 11, p. 217 - 295). Elsevier. doi: https://doi.org/10.1016/B978-0-12-460811-5.50010-6

Tichelaar, B. W., & Ruff, L. J. (1989, May). How good are our best models? Jackknifing, bootstrapping, and earthquake depth. *Eos, Transactions American Geophysical Union*, *70*(20), 593–606. doi: 10.1029/89EO00156

Vallée, M., Lands, M., Shapiro, N. M., & Klinger, Y. (2008). The 14 November 2001 Kokoxili (Tibet) earthquake: High-frequency seismic radiation originating from the transitions between sub-Rayleigh and supershear rupture velocity regimes. *Journal of Geophysical Research: Solid Earth*, *113*(B7). doi: 10.1029/2007JB005520

Veen, B. D. V., & Buckley, K. M. (1988, April). Beamforming: a versatile approach to spatial filtering. *IEEE ASSP Magazine*, *5*(2), 4–24. doi: 10.1109/53.665

Wald, D. J., & Heaton, T. H. (1994). Spatial and temporal distribution of slip for the 1992 Landers, California, earthquake. *Bulletin of the Seismological Society of America*, *84*(3), 668.

Wang, D., Chen, Y., Wang, Q., & Mori, J. (2018, May). Complex rupture of the 13 November 2016 Mw 7.8 Kaikoura, New Zealand earthquake: comparison of high-frequency and low-frequency observations. *Tectonophysics*, *733*, 100–107. doi: 10.1016/j.tecto.2018.02.004

Wang, D., Takeuchi, N., Kawakatsu, H., & Mori, J. (2016). Estimating high frequency energy radiation of large earthquakes by image deconvolution back-projection. *Earth and Planetary Science Letters*, *449*, 155 - 163. doi: https://doi.org/10.1016/j.epsl.2016.05.051

Wang, J., & Teng, T.-l. (1997, October). Identification and picking of S phase using an artificial neural network. *Bulletin of the Seismological Society of America*, *87*(5), 1140–1149.

Wang, R. (1997). Tidal response of the solid Earth. In H. Wilhelm, W. Zürn, & H.-G. Wenzel (Eds.), *Tidal phenomena* (pp. 27–57). Berlin, Heidelberg: Springer Berlin Heidelberg. doi: 10.1007/BFb0011456

Wang, T., Wei, S., Shi, X., Qiu, Q., Li, L., Peng, D., … Barbot, S. (2018). The 2016 Kaikōura earthquake: simultaneous rupture of the subduction interface and overlying faults. *Earth and Planetary Science Letters*, *482*, 44-51. doi: 10.1016/j.epsl.2017.10.056

Wang, X., Ding, Z., & Ma, Y. (2017). Rapidly tracking the rupture energy center of the Mw7.9 Nepal earthquake by using nonlinear array stacking method. *Chinese Journal of Geophysics*. doi: 10.6038/cjg20170112

Wen, Y.-Y., Ma, K.-F., & Fry, B. (2018). Multiple-fault, slow rupture of the 2016 Mw 7.8 Kaikōura, New Zealand, earthquake: complementary insights from teleseismic and geodetic data. *Bulletin of the Seismological Society of America*. doi: 10.1785/0120170285

Wessel, P., Smith, W. H. F., Scharroo, R., Luis, J., & Wobbe, F. (2013). Generic Mapping Tools: improved version released. *Eos, Transactions American Geophysical Union*, *94*(45), 409–410. doi: 10.1002/2013EO450001

Wittlinger G., Herquel G., & Nakache T. (1993). Earthquake location in strongly heterogeneous media. *Geophysical Journal International*, *115*(3), 759–777. doi: 10.1111/j.1365-246X.1993.tb01491.x

Xu, Y., Koper, K. D., Sufri, O., Zhu, L., & Hutko, A. R. (2009). Rupture imaging of the Mw 7.9 12 May 2008 Wenchuan earthquake from back projection of teleseismic P waves. *Geochemistry, Geophysics, Geosystems*, *10*(4). (Q04006) doi: 10.1029/2008GC002335

Yao, H., Gerstoft, P., Shearer, P. M., & Mecklenbruker, C. (2011). Compressive sensing of the Tohoku-Oki Mw 9.0 earthquake: frequency-dependent rupture modes. *Geophysical Research Letters*, *38*(20). (L20310) doi: 10.1029/2011GL049223

Zelt, C. A., & Ellis, R. M. (1989, May). Seismic structure of the crust and upper mantle in the Peace River Arch Region, Canada. *Journal of Geophysical Research: Solid Earth*, *94*(B5), 5729–5744. doi: 10.1029/JB094iB05p05729

Zhang, H., & Ge, Z. (2010). Tracking the rupture of the 2008 Wenchuan earthquake by using the relative back-projection method. *The Bulletin of the Seismological Society of America*, *100*, 2551-2560. doi: 10.1785/0120090243

Zhang, H., Koper, K. D., Pankow, K., & Ge, Z. (2017). Imaging the 2016 Mw 7.8 Kaikoura, New Zealand, earthquake with teleseismic P waves: a cascading rupture across multiple faults. *Geophysical Research Letters*, *44*(10), 4790–4798. (2017GL073461) doi: 10.1002/2017GL073461

Zhou, H. (1994). Rapid three-dimensional hypocentral determination using a master station method. *Journal of Geophysical Research: Solid Earth*, *99*(B8), 15439–15455. doi: 10.1029/94JB00934